Instituto Politécnico de Lisboa

Instituto Superior de Engenharia de Lisboa

Escola Superior de Tecnologia de Saúde de Lisboa

Development of a Liquid Cell to Study the Release of Brimonidine in Real Time

Tiago Alves Pereira

Thesis to obtain the Master of Science Degree in Biomedical Engineering

Supervisors:

Dr. Quirina Ferreira (Instituto de Telecomunicações)

Prof. Dr. Manuel Matos (Instituto Superior de Engenharia de Lisboa)

December 2019

Instituto Politécnico de Lisboa

Instituto Superior de Engenharia de Lisboa

Escola Superior de Tecnologia de Saúde de Lisboa

Development of a Liquid Cell to Study the Release of Brimonidine in Real Time

Tiago Alves Pereira

Thesis to obtain the Master of Science Degree in Biomedical Engineering

Supervisors:

Dr. Quirina Ferreira (Instituto de Telecomunicações)

Prof. Dr. Manuel Matos (Instituto Superior de Engenharia de Lisboa)

Examination Committee:

Chairperson: Prof. Dr. Cecília Calado (Instituto Superior de Engenharia de Lisboa)

Supervisor: Dr. Quirina Ferreira (Instituto de Telecomunicações)

Member of the Committee: Prof. Dr. Maria de Fátima Raposo (Faculdade de Ciências e Tecnologia)

December 2019

“Mais vale uma hora de coragem que um dia de preguiça”

- Cristina Alves

Acknowledgments

Gostaria de usar esta página para agradecer a todos os que me ajudaram neste percurso, de forma direta ou indireta, mas sem elas não teria chegado ao fim de certeza!

Um agradecimento especial aos meus orientadores nesta tese, Doutora Quirina Ferreira e Professor Doutor Manuel Matos, pela ajuda fundamental para a realização deste trabalho, não só pela excelente orientação durante todo o percurso de criação do projeto, mas também pela adaptação incansável aos meus horários de trabalho, que nem sempre eram os mais fáceis. Desde já, um enorme obrigado!

Quero agradecer ao grupo de Química do Instituto Superior de Engenharia de Lisboa por me cederem o espaço para a montagem da impressora 3D, e ao Instituto Superior Técnico, por me deixar realizar grande parte das experiências laboratoriais nas suas instalações, fornecendo-me todos os equipamentos que necessitava para a realização deste projeto.

Quero agradecer ao Doutor Fabrice Cousin, do Laboratório Léon Brillouin em França, por ter entrado em contacto e se ter disponibilizado a realizar a análise dos filmes de multicamadas através da técnica de Refletividade Especular de Neutrões.

Um obrigado a todos os meu colegas de laboratório, por me explicarem como eram e funcionavam, sempre disponíveis para me ajudarem quando tive mais dificuldades. Quero agradecer também às minhas colegas de trabalho, por me terem facilitado nos horários e me substituírem sempre que precisava de ir ao laboratório. A todas vocês, um grande obrigado.

Agradeço a todos os meus colegas de Mestrado, especialmente aos meus “manolas” e membros do IEEE, que apesar do pouco tempo que passamos junto nesta reta final que é a tese, não deixaram de ser uma parte fundamental de toda a viagem.

Aos meus amigos de longa data, que no fundo não me ajudaram muito, no que diz respeito à elaboração da tese, mas que estavam sempre prontos para um fundamental “cafezinho e bowling” ao fim-de-semana, e só por isso, merecem um agradecimento.

À Marisa, um especial agradecimento, pelo apoio incondicional, por toda a ajuda impagável que me deste, por acreditares em mim, por estares sempre presente na minha vida, antes longe e agora perto. Pela contínua demonstração de amor, o meu maior obrigado!

Por fim, agradeço à minha família, o meu maior suporte antes, agora e sempre. Sem vocês, nunca teria conseguido. Obrigado, Mãe, Pai e Karicas, espero que se orgulhem de mim como eu de vocês.

Development of a Liquid Cell to Study the Release of Brimonidine in Real Time

Tiago Alves Pereira

2019

The present work was primarily conducted in the Organic Electronics laboratory of the Instituto de Telecomunicações through a collaboration protocol established between Instituto Superior Técnico and Instituto Politécnico de Lisboa.

Abstract

The experimental method usually used to monitor a drug release is not always representative of the natural conditions under which this process occurs. In most of the cases, the study of drug release kinetics is a static process that is unaffected by the fluid dynamics that occur in all living organisms.

In this thesis, a dynamic cell was developed to quantify the release of Brimonidine, a drug used in the treatment of glaucoma, from a thin nanostructured film in real time. More specifically, the design and subsequent 3D printing of a dynamic cell under a constant flow of an aqueous solution was made to monitor the release of Brimonidine.

For the present work, multilayer films composed of Brimonidine encapsulated in Polymer β-cyclodextrin alternated with a water-soluble polymer, poly-β-amino ester were prepared by the layer-by-layer technique and their growth was controlled by Ultraviolet-Visible Spectroscopy, Atomic Force Microscopy and Neutron Reflectivity

Brimonidine release kinetics were monitored in the dynamic cell immersing the films in a volume of about 25 cm^3 under the influence of two flow rates: Q= 4.14 mL/min and Q=2 mL/min. Samples were collected at specific times and analyzed by Ultraviolet-Visible spectroscopy. Results demonstrated a stratified release of Brimonidine at both flow rates, where each step corresponded to the release of a bilayer. The kinetics have been found to be slower for the lower flow rate. This work demonstrated the relevance of using a dynamic drug release control system that can be used in other drug delivery systems.

Keywords: Drug delivery system, Dynamic cell, 3D printing, Brimonidine, Layer-by-layer technique.

Resumo

O método experimental para a monitorização da libertação de um fármaco nem sempre é representativo das condições naturais em que este processo ocorre. Na maior parte dos casos, o estudo da cinética de libertação de um fármaco ocorre de forma estática, sem sofrer influencia das dinâmicas de fluidos que se encontram presentes em qualquer organismo vivo. Nesta tese desenvolveu-se uma célula que permite quantificar a libertação de Brimonidina, fármaco usado no tratamento do glaucoma, a partir de filmes finos e nanoestruturados em tempo real. Mais especificamente, foi feito o projeto e posterior impressão 3D de uma célula dinâmica que serviu como suporte para os filmes criados com a Brimonidina serem sujeitos uma solução aquosa com um fluxo dinâmico e caudal ajustável.

Para o presente trabalho, filmes de multicamadas compostos por Brimonidina encapsulada em polímero de β-ciclodextrina e alternadas com um polímero hidrossolúvel, poli-β-amino-éster (PBAE) foram preparados pela técnica de camada sobre camada e o seu crescimento foi controlado por Espectroscopia de Ultravioleta-Visível, Microscopia de Força Atómica e Reflectividade de Neutrões

A cinética de libertação da Brimonidina foi monitorizada na célula impressa com um volume de cerca de 25 cm^3 sob a influência de dois caudais: 4.14 mL / min e 2 mL / min. As amostras foram recolhidas em tempos específicos e analisadas por Espectroscopia de Ultravioleta-Visível. Os resultados demonstraram uma liberação estratificada de Brimonidina em ambos os caudais, onde cada etapa correspondia à libertação de uma bicamada. Verificou-se que a cinética é mais lenta para o caudal mais baixo. Com este trabalho demonstrou-se a importância de usar um sistema dinâmico para o controlo da libertação de fármacos onde é possível observar uma libertação passo por passo e pode ainda ser usado para outros sistemas semelhantes.

Palavras-chave: Sistema de entrega de fármaco, Célula dinâmica, Impressão 3D, Brimonidina, técnica de camada-sobre-camada.

Contents

List of Figures

List of Tables

Nomenclature

A	Absorbance
AH	Aqueous humor
AFM	Atomic Force Microscopy
Brim	Brimonide
CAD	Computer-based design
CL	Contact lenses
CD	Cyclodextrins
DD	Drug delivery
DDS	Drug delivery systems
Q	Flow rate
FDM	Fused deposition modelling
GDD	Glaucoma drainage devices
GON	Glaucomatus optic neuropathy
IOP	High intraocular pressure
ISEL	Instituto Superior de Engenharia de Lisboa
LbL	Layer-by-layer
Mw	Molecular weight
NBSIMR	National Bureau of Standards Institute for Materials Research
NR	Neutron reflectivity
PBS	Phosphate Buffer Saline
PZT	Piezoelectric
PBAE	Poly(β-amino ester)
PLA	Polylactic acid
PSPD	Position sensitive quadrant photodiode
RPR	Renewal percentage rate
Re	Reynolds coefficient
Rms	Root-mean-square
STL	Standard Triangle Language
THF	Tetrahydrofuran
UV-Vis	UV–visible spectroscopy

Chapter 1 – Introduction

1 Introduction

This chapter gives a short state of art of glaucoma treatments and its improvement using nanostructured drug delivery films. A brief introduction about drug delivery films is given followed by a description of the methodologies to follow the amount of drug released to an aqueous environment based on static and dynamic setup.

1.1 Ocular devices for glaucoma treatment

According to the World Health Organization, glaucoma is a progressive optic neuropathy found to be the leading cause of irreversible blindness worldwide (1). Glaucoma is defined by a depletion of retinal ganglion region and atrophy of the optic nerve, usually associated with high intraocular pressure (IOP) in open-angle glaucoma (2, 3). This is the result of a blockage, which leads to insufficient drainage of the aqueous humor (AH), increasing internal pressure, damaging the surrounding nerves, vessels and cells as can be seen in Figure 1.

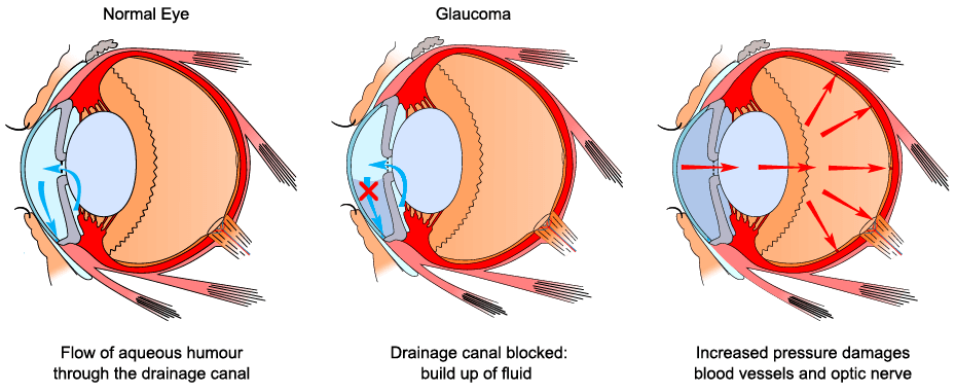

Figure 1 –Schematic representation of a normal IOP eye and a high IOP eye (https://www.sugikiportis.com/glaucoma-honolulu/glaucoma-diagram-1000 / 2019/07/19).

The main characteristic of Glaucomatus optic neuropathy (GON) is the evolution of the retinal depletion and optic nerve atrophy, which leads to a progressive peripheral vision loss, decrease in contrast sensitivity and diminished central visual acuity (VA) (Figure 2) (4). The problem affects more than 70 million people worldwide, with approximately 10% being bilaterally blind. It is estimated that near 11 million people will suffer from total blindness by the year 2020 (5).

Figure 2 – Comparative representation of a normal visual field (left image) and a glaucoma-affected visual field (right image), (https://drjai.com.au/glaucoma-treatment-bundaberg/ 2019/07/20).

The development of glaucoma is strongly influenced by genetics and age. The risk of developing glaucoma increases exponentially after the age of 40 in strong association with high IOP (5).

Most of the therapies applied nowadays are focused on decreasing IOP, in order to decrease the disease progression (6). Topical IOP treatment remains the best method applied to all types of glaucoma (7). The majority of ocular treatments (i.e. about 90%) are in eye drops form (8). One of the most effective anti-glaucoma drugs is Brimonidine. This drug is rapidly absorbed and its capacity to effectively decrease IOP has been proven in clinical trials, increasing the aqueous humor flow from 40% to 67% in 4 hours (9). Brimonidine is equally or even more effective than others marketed anti-glaucoma drugs, managing to increase AH drainage, while decrease its production (8, 9). The most common and simpler posology for Brimonidine is via topical eye drops, three times per day (10).

However, highly concentrated solutions are required to reach the therapeutic level intended, in order to overcome the natural defenses mechanisms, which have influence on drug's efficiency (11). The natural barrier created by the three lacrimal layers film in association with the reactive blinking reflex created by the falling drop, leads to the elimination of a large percentage of the drug by nasolacrimal drainage and evaporation, losing 80% to reflective tearing and nasolacrimal drainage within 5 minutes after application (12). From the remaining 20%, only 3% to 5% of the drug penetrates the cornea and reach the final target sites (10, 13).

Furthermore, studies showed that the low commitment and poor maintenance of self-administration schedule represents a major factor for the inefficiency of topical eye drops and poor IOP control (10). Over 50% of the patients were non-compliant and 35% demonstrated improper administration technique, in most cases, due to arthritis, osteoarthritis and other aging related diseases (14).

To overcome these issues, new drug delivery systems (DDS) with easy application, effective target delivery and dose accuracy are needed (15). Nanotechnology-base ocular devices and glaucoma drainage techniques are being developed in order to remove the compliance factor out of the equation as well decreasing Brimonidine concentration required (Figure 3) (15).

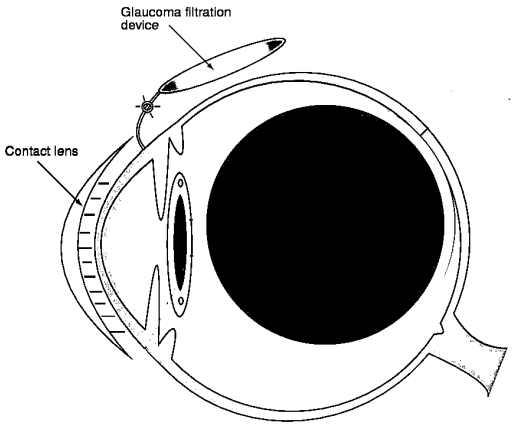

Figure 3 - Schematic representation of a contact lens and glaucoma valve for drug delivery in the eye.

The use of soft contact lenses (CL) impregnated with an antiglaucoma drug was an important step in the development of this DDS (15). In earlier stages, the lens was soaked with the anti-glaucoma drug and placed in the eye, resulting in a better drug release profile and better patient compliance by the improvement of the VA. However, the simple soaking of the lens into the anti-glaucoma drug results in a maximum release-time of 2 hours, needed to be re-soaked constantly (16, 17).

The use of nanoparticles for the encapsulation of the anti-glaucoma drug into the CL matrix, allowed a significant improvement in the loading drug capacity, lowering the levels wasted drug and a more sustainable release over time (16, 18). Recently, Sun *et al.* (2017) using a Brimonidine loaded CL nanoparticles with 125.0 μg/g of Brimonidine, showed a continuous drug release up to 144h, with good corneal biocompatibility (19). Similar to the CL, nanopatchs and fornix inserts have been developed as a new form of corneal DDS, with the advantage of lowering the risk of foreign body sensation and inflammation potentially caused by the CL (15). With a drug capacity greater than CL, Franca *et al.* (2014), was able to create a conjunctival fornix insert, with a sustained *in vitro* drug release of 8h and a significant IOP reduction for 4 weeks, after one single application (15, 20).

This thesis aims to develop multilayer DD films composed of layers of Brimonidine encapsulated in polymer-β-cyclodextrin (Poly-CD+Brim) alternated with a barrier layer which controls the release of a drug and composed of poly-β-amino ester (PBAE). These films were previously developed in the research group of Organic Electronics of IT (21-23) and it was observed that the PBAE delay the drug release ensuring a precise drug amount delivery.

However, it was observed that the methodology based on a static setup used to follow the Brimonidine release to the aqueous environment did not allow its correct monitorization. In this thesis, a dynamic system was developed and tested in order to mimic the biologic conditions of the ocular dynamic fluids. Both methods, static and dynamic, are explained throughout this work.

1.2 Nanostructured Drug delivery films

By definition, a DDS can be a formulation or a device with the purpose of introducing a therapeutic substance into the body. It is designed to improve the pharmacological and therapeutic properties of the drug administered parenterally (24), by controlling the drug release time, rate and place, minimizing side effects and frequency of administration (25). Drugs can be introduced into the human body by various anatomical routes, depending on the effect intended. The route of administration choice depends on the disease, the effect desired and the product available (26).

DDS is a very effective and efficient performance on-spot delivery, reducing the required doses to trigger a reaction, improving upon side effects created by conventional administration, resulting in less drug waste and higher levels of patient compliance (27).

Layer-by-layer is a simple and versatile method for the construction of DDS, allowing the fabrication of complex and functional multilayer films. The LbL technique is a cyclical process based in the adsorption of a charged material onto a substrate, followed by a washing step and then a new adsorption of an oppositely charged material on the top of the first layer. This process can be repeated until the multilayer film reaches the desired thickness. Films can be formed through electrostatic interactions, covalent interactions, hydrogen bonding, host-guest, and others. (28, 29). By changing the concentration of components, pH, immersion time and ionic strength, it is possible to adjuncts and fine-tune the films in order to be used in a wide range of biomedical applications (30, 31).

There are several methods of LbL assembly, for example, dipping (32), spinning (33), spraying (34), electrodeposition (35), between others, which have different input materials and different assembly technologies. Assembly technologies can be divided into five groups: immersive, spin, spray, electromagnetic and fluidic. The assembly method has a direct influence on the physicochemical properties of the films, for example, on film's thickness, homogeneity and structure. Therefore, method's choice must be made not only considering process properties, as time, scalability and automation, but also the desired properties of the film.

Immersive or dip LbL assembly, which was the method used in this work (Figure 4), is the most widely used method and it is based on the immersion of a substrate into a solution composed by the desired material and also washing steps to remove the unbound material (32, 36). Immersive assembly is widely used for the formation of thin films, once it creates more homogeneous surfaces, when compared with non-LbL assembly (37). This technology is simple and easily accessible, using simple substrates with several shapes or sizes.

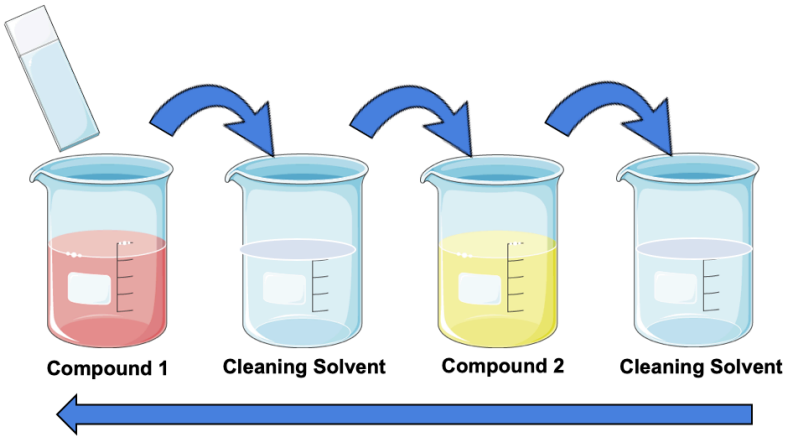

Figure 4 - Schematic representation of the LbL method.

The method used in this work was previously studied and optimized in the previous thesis (21). The layers configuration and adsorption times for each layer are already defined. The procedure is based in dipping a clean quartz substrate into a solution of charged polymers. After each submersion in the polymer solution (compound 1 and compound 2 in Figure 4), a washing step is necessary to remove supernatant material (cleaning solvent in Figure 4), ensuring a homogeneous layer (38). The procedure must be repeated as many times as necessary until the desired number of layers is achieved. The formation of one bilayer is composed by the four steps as schematized in Figure 4.

1.3 Drug delivery kinetic in a static system

In the previous thesis (21, 22), the drug delivery kinetic was study in a static form. The LbL films were immersed in a beaker with a Phosphate Buffer Saline (PBS) solution at 37ºC, with a 7.4 pH and salts concentration levels like those found in human biological fluid. Despite the aqueous solution was under agitation and the fluid was periodically replaced by a new one, this setup does not represent the real dynamic which occurs in human body mainly on the eye. This fluid dynamics influences the drug release and a static setup is not representative of real condition. It was observed (21, 22) using a static setup occurs a

significant salts accumulation on the top of a film resulting from the buffer solution which affects the drug release. In order to overcome this problem, it was developed under this thesis a dynamic setup which allows the monitorization of drug release in real time.

1.4 Motivation

In the previous research works (21, 22), a static kinetic system was used to testing the adsorption of the drug delivery (DD) film synthetized by the LbL technique. Consequently, the salts of the phosphate buffer saline used rapidly formed agglomerates on the film surface, interfering with the spectra measurements and making impossible to obtain reliable DD film absorbance results.

In order to solve this problem, a new setup to study the Brimonidine release was developed, preventing the agglomerate of salts on the film surface. A dynamic cell was developed allowing the continuous flow of the aqueous solution where the film is immersed. The developed cell is original and it was designed and fabricated during this thesis. It allowed to mimic the ocular environment that is more realistic considering that the drug that was studied (Brimonidine) is to be delivered in the intraocular region with a continuous flow of aqueous humor. This setup may be further implemented in other laboratory studies which involves drug delivery systems.

1.5 Objectives

The main objective of this research is to create a dynamic cell for the real-time study of Brimonidine release.

In more detailed point-by-point analysis, the objectives are:

- Creating a dynamic cell prototype using the TinkerCAD® software design program.
- Printing the prototype cell using the HelloBeePrusa® 3D printer previously assemble.
- Preliminary tests using aqueous solutions of $K_2CR_2O_7$to e valuate the dynamic cell and to optimize its design.
- Preparation of the DD LbL films, consisting of a Polymer β-cyclodextrin (Poly-

CD) encased Brimonidine monolayer alternating with a PBAE monolayer.

- Characterization of the growth of DD films using Ultraviolet-Visible (UV-Vis) Spectroscopy, Atomic Force Microscopy (AFM) and Neutron Reflectivity (NR).
- Characterization of Brimonidine kinetic using the fabricated dynamic cell evaluating the influence of two different flow rates – Q = 4 mL/min and Q = 2 mL/min.

1.6 Thesis Outline

This thesis is divided in six Chapters. Chapter 1 contains the Introduction, where the state of the art of the work is presented, addressing themes regarding glaucoma and its complications and the recent developments which involves new therapeutics based on nanodevices.

Chapter 2 describes the materials used to print the dynamic cell and preparation of DD films. It also includes the methods of multilayer films preparation, dynamic cell fabrication and the preliminary tests to optimize its design. All the characterization techniques used to monitoring the film growth and the Brimonidine release are also described in this chapter.

Chapter 3 presents the results about the multilayer films growth and its characterization with UV-Vis spectroscopy, AFM and NR.

Chapter 4 includes the results of the Brimonidine release kinetics.

Chapter 5 describes the main conclusions of this work and the Chapter 6 includes the proposal for future work following the results of this project.

The Appendix section is presented at the end with additional graphs and results.

Figure 5 resumes the thesis outline.

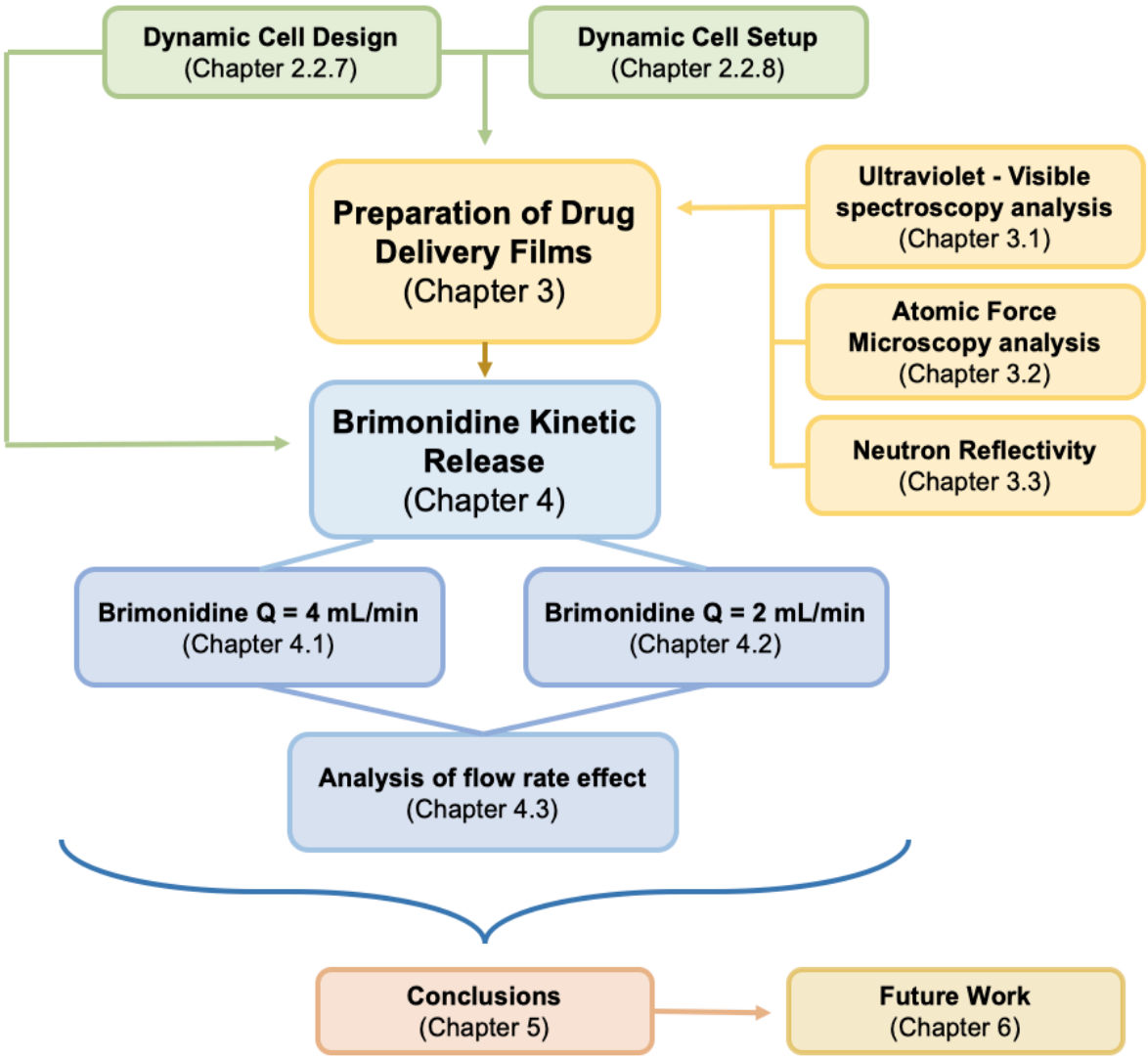

Figure 5 - Schematic representation of thesis outline.

Chapter 2 – Materials and Methods

2 Materials and Methods

2.1 Materials

This sub-chapter describes the materials used to prepare the multilayer films, namely the Poly-CD encapsulation protocol used to encapsulate Brimonidine molecules, PBAE synthesis and lastly the Sodium acetate trihydrate solution preparation, used as a solvent as well as the aqueous solution for dynamic release in 3D printed cell. All the materials presented are described in greater detail in (21).

2.1.1 β-cyclodextrin Polymer

Cyclodextrins (CD) are cyclic oligosaccharides, in the form of a macrocyclic ring, with six α-D-glucopyranose units connected by α-(1, 4) glycosidic bonds (Figure 6) (39).

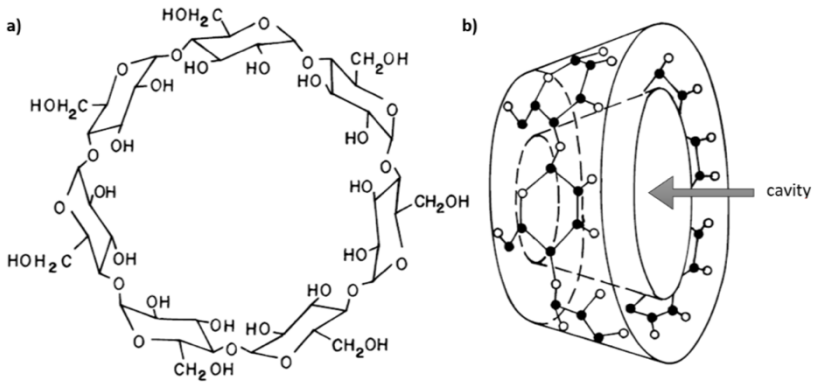

Figure 6 – Chemical structure (a) and three-dimensional structure (b) of cyclodextrin, figure adapted from (46).

The spatial conformation combined with the lipophilic inner cavity and hydrophilic outer surfaces, make it ideal for a DD system, forming noncovalent inclusion complex and improving the solubility of the drug. (40-42). Poly-CD is an ideal polymer for the creation of multilayer DD films, once Poly-CD is able to bind to Brimonidine, forming stable complex, with high ocular biocompatible properties and very low toxicity and cytotoxicity.

Polymer β-cyclodextrin was obtained from Sigma Aldrich (Molecular weight (Mw) = 2.000 to 3.000 Da). The molecular structure is show in Figure 7.

To obtain the Poly-CD solution, the power was dissolved in the sodium acetate solution and stirred for 30 minutes, then it was placed in ultrasound bath for 5 to 15 minutes at room temperature, to ensure the dissolution of all powder particles.

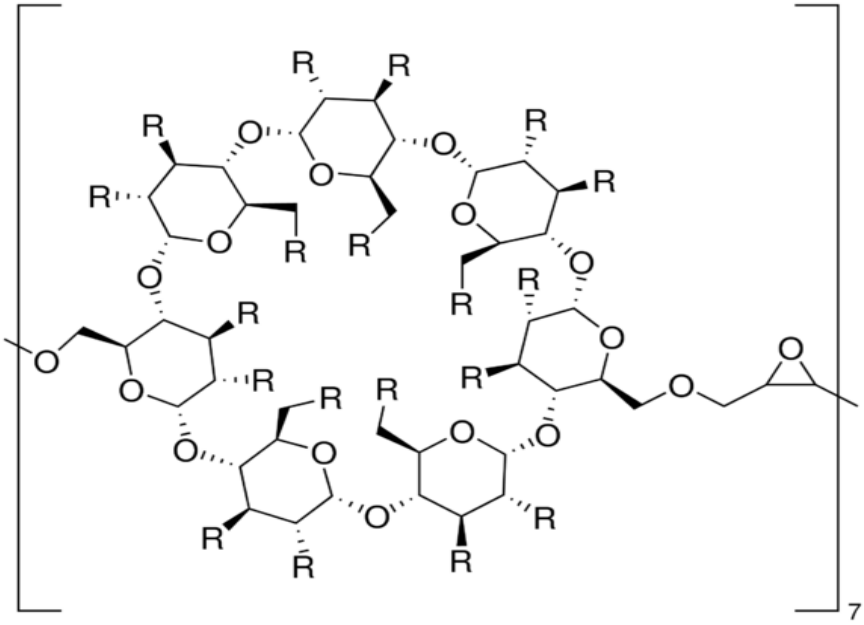

Figure 7 - Poly β-cyclodextrin molecular structure, figure adapted from ((43)).

2.1.2 Poly (β-amino ester)

Poly (β-amino ester) (PBAE) refers to a cationic polymer, synthesized by Michael addition polymerization of an amine and an acrylate monomer (44). Presenting high biodegradability by hydrolysis and high pH responsiveness. This non-viral vector offers advantages over viral vectors, such as easy production, stability, low immunogenicity and toxicity (45).

PBAE was synthetized in the Organic Electronics group of the Instituto de Telecomunicações. PBAE used was done for the previous work and it's described in greater detail in (21, 22) as reference earlier.

The synthesis is based on the protocol described by Lyn *et al.* (44), consisting of adding 4,4'-trimethylenedipiperidine (97% purity, Sigma Aldrich, CAS number 16898-52-5) to 1,4-butanediol diacrylate (99% purity, Alfa Aesar, CAS number 1070-70-8), distilled and mixed in dry tetrahydrofuran (THF), allowing the copolymerization of the monomers. The resulting PBAE polymer was then purified by diethyl ether precipitation and left in vacuum. The final form of purified PBAE is shown in Figure 8. The layers of PBAE used in the multilayer film are deposited alternately with Poly-CD layers, serving as the anchor point of these molecules.

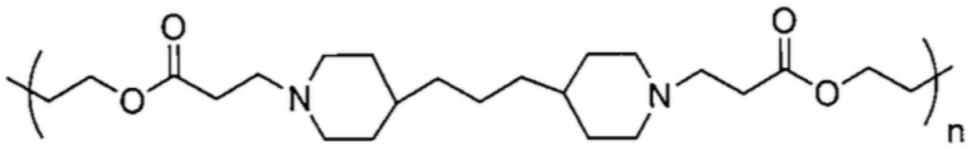

Figure 8 – Final PBAE form, after precipitation in diethel ether and vacuum drying in a Buchner funnel, figure adapted from (44).

2.1.3 Brimonidine

Brimonidine is an alpha2-adrenergic agonist (Figure 9) that inhibits the adenylate cyclase enzyme and suppresses the formation of cAMP-dependent, increasing the uveoscleral outflow and decreasing the aqueous humor production at the same time (46, 47).

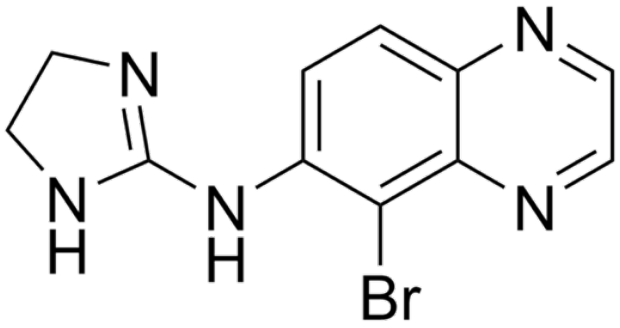

Figure 9 – Chemical structure of Brimonidine.

The half-life of Brimonidine is 2.5 hours, being primarily metabolized in the liver and then expelled through the urinary track, along with its metabolites (48).

The Brimonidine powder was obtained from Sigma Aldrich (M_w=292.13 g/mol, CAS number 59803- 98-4). As previously mentioned in Chapter 1, Brimonidine is a drug used to reduce intraocular pressure in patient with glaucoma.

2.1.3.1 Brimonidine encapsulation

Brimonidine encapsulation consist in creating a molecular complex with Poly-CD, improving its physicochemical properties and molecular stability, for posterior formation of multilayer films. The encapsulation starts with the dissolution of Brimonidine, at its maximum solubility value of 0.8 mg/mL, into a solution of Poly-CD. The molar ratio of the complex is 1:1 and it is formed through the binding of one molecule of Brimonidine with one molecule of CD, as it can be seen in Figure 10 (42, 49, 50).

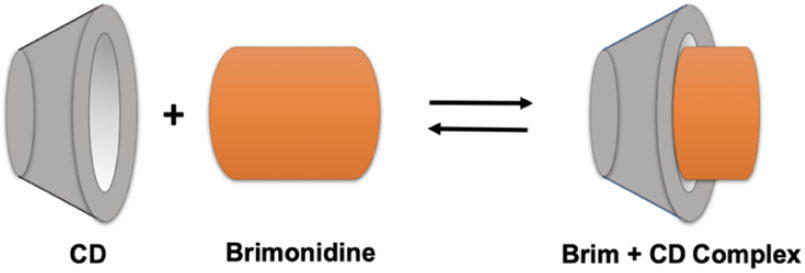

Figure 10- Schematic illustration of a 1:1 complex formed by one molecule of CD and one of Brimonidine (Brim).

The solution was then stirred for 48 hours, until all the precipitated drug at the bottom of the flask has been dissolved and the full encapsulation of Brimonidine within Poly-CD (Poly-CD + Brim) was obtained.

The mixture was then diluted again in Poly-CD in order to obtain a concentration of 2 mM (the same as the films previously created (21, 22)).

2.1.4 Sodium acetate trihydrate

Sodium acetate trihydrate (with a Weight-average molecular weight (M_w) of 136.08 g/mol) was obtained from Alfa Aesar, CAS number 6131-90-4.

The sodium acetate powder was dissolved in milli-Q water and stirred, forming a solution with the concentration of 100 mM. Then the solution was used as a solvent for the polymer solutions that form the multilayer DD films as well as for washing substrates during films preparation. For the washing solution, pH adjustment was performed with glacial acetic acid until optimal value of pH 5. The whole process was carried out at room temperature. The same solution was also used as the phosphate buffer saline (PBS) for all experiments performed, at 7.4 pH and at room temperature.

2.2 Characterization techniques and methods

This sub-chapter describes the techniques used to follow the films growth and the drug released. More specifically, UV-Vis Spectroscopy was used to characterize the film growth and the Brimonidine released to the aqueous solution. AFM technique was used to characterize the surface of each film's bilayer and the Neutron Reflectivity technique was used to analyze the thickness of each layer. This sub-chapter also describes the preliminary tests that were made to optimize the design cell and all steps which involved its fabrication.

2.2.1 Ultraviolet-Visible spectroscopy

UV–Vis spectroscopy is based on the interaction of the light with the matter, mainly on the measurement of the ratio between transmitted light and incident light, in the wavelength range between the ultraviolet and visible light (51). This technique allows the quantitative analysis of compounds, depending on molecules absorption.

Lambert-Beer´s law relates the attenuation of light to the properties of the solution that the light is interacting, allowing the quantitative measurement of the concentration of the absorbing specie, using the equation:

$$\log\left(\frac{I_0}{I}\right) = A = e.c. \qquad \textbf{Equation (1)}$$

Where I_0 is the initial intensity of the light entering the sample, I is the remaining beam intensity, A is the absorbance, e is the molar attenuation coefficient or absorptivity of the attenuating species in the material sample, c is the concentration of the light absorbing substance and l is the pathlength of the sample in cm (52, 53).

The spectrophotometer measures I_0 and I and the ratio of I / I_0 is the transmittance, usually expressed in percentage ($\%T$). the absorbance is related with the transmittance by:

$$A = -\log\left(\frac{\%T}{100\%}\right) \qquad \textbf{Equation (2)}$$

The main components of a spectrophotometer includes: a radiation source, previously selected by the operator, which limits the spectrum to the region of interest; a prism to separate the different wavelengths of the light; two sample containers, one for the sample and other for the reference, being the reference beam intensity taken as 100% Transmission; a detector, which detects the radiation after the attenuation of light by the sample; a computer module for processing the signal (53).

Using this technique, the absorption spectra of the DD film were obtained to follow the film growth after the formation of each bilayer and to analyze the Brimonidine release. For the film growth monitorization, the spectra were obtained between 190 nm and 900 nm wavelength, with a velocity of 25 nm/s and a PBS solution at 5 pH as a reference.

For the kinetics release test, a wavelength rage from 190 nm to 900 nm as used with a velocity of 5 nm/s and PBS solution at 7.4 pH as reference. All the absorption spectra of the films were obtained using quartz substrate. A Cecil Aquarius CE 7200 spectrophotometer in the Organic Electronics group at Instituto de Telecomunicações was used to characterize all solutions and DD films (Figure 11).

Figure 11 –UV-Vis Cecil Aquarius CE 7200 spectrophotometer.

2.2.2 Ultraviolet-Visible spectroscopy *in-situ* test measurements

Preliminary tests were performed to verify the spectrophotometer with a standard substance, potassium dichromate ($K_2Cr_2O_7$), used by the National Institute of Standards and Technology (NIST) (54). The recommend four main wavelengths used correspond to maximum and minimum absorbance in the spectrum, at 235, 257, 313 and 350 nm, to be used for checking the accuracy of the absorbance scale of narrow bandpass spectrophotometers, mainly because of its well defined regions (Figure 12) (54).

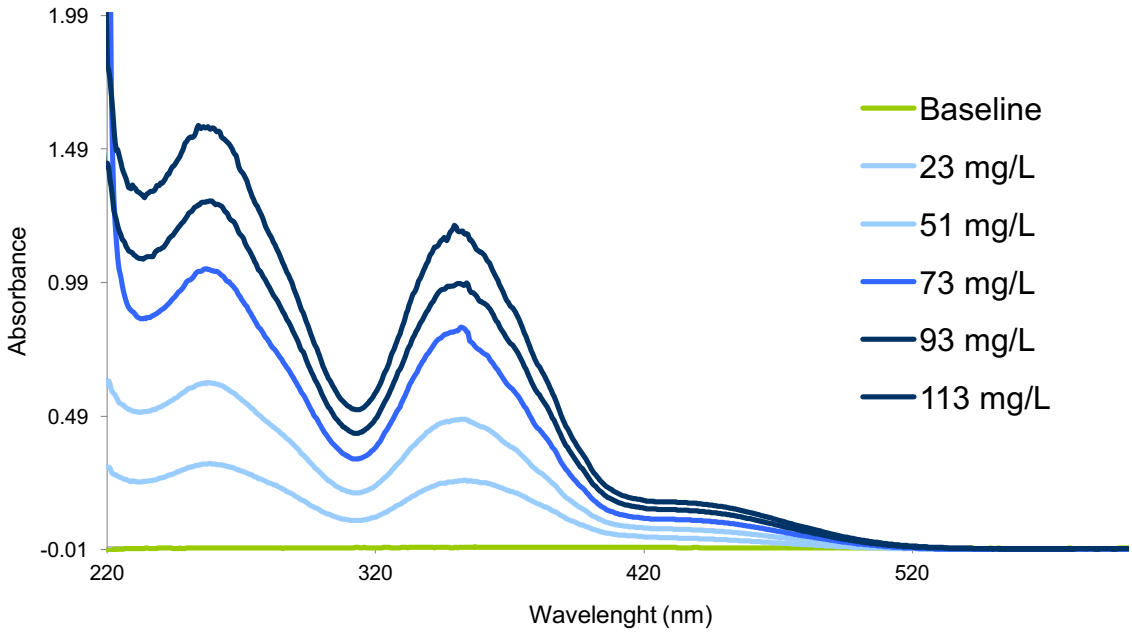

Figure 12 - Absorption spectrum of K_2CrO_7 at different concertation values.

Five solutions were prepared in volumetric flasks containing 23 mg/L, 51 mg/L, 73mg/L, 93mg/L and 114 mg/L of $K_2Cr_2O_7$, the recommend by the NIST (54). To create a calibration curve, the wavelength selected was 313 nm, which is the minimum absorbance peak. The

use of the minimum peak is justified by the fact that the maximum wavelength of 235 nm is subjected to interferences provoked by the use of plastic cells instead of quartz cells. In the case of the second maximum peak, at 257 nm wavelength, this was affected by a specific mechanical characteristic of the spectrophotometer, that exchanges the use of a deuterium lamp (used in lower wavelengths) by another deuterium lamp (used in higher wavelengths), which occur between 250-260 nm, creating a false noise peak, making the measurement of the absorbance at this point unreliable.

Using the Microsoft Excel® tool, the absorbance values obtained at the 313 nm wavelength in each different concentration spectrum of $K_2Cr_2O_7$ were used to create a calibration, as show in Figure 13 and Table 1.

The resulting calibration curve was adjusted with a linear function, expressed visually by the blue line on Figure 13. The calculation of the $K_2Cr_2O_7$ unknown concentration in the samples from the values of the absorbance is given by the function:

$$y = m \times x \;\; (=) \;\; A = m \times \log\left(\frac{I_0}{I}\right) \qquad \textbf{Equation (3)}$$

Where m is the slope of the line, that describes the slant, in this case, 0.0045. This principle can equally be applied when using Brimonidine instead.

Table 1 - *Concentration table of $K_2Cr_2O_7$ in relation to the absorbance value*

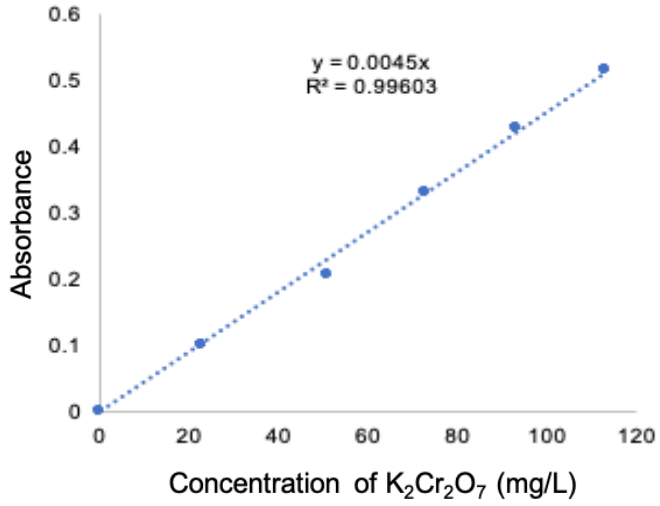

mg/L	Absorbance
0	0
23	0,099
51	0,204
73	0,33
93	0,426
113	0,515

Figure 13 *– Concentration graph of $K_2Cr_2O_7$ in relation to the absorbance value.*

2.2.3 Atomic Force Microscopy

The Atomic Force Microscope (AFM) is a high-resolution scanning probe microscope able to measure at resolution in the order of a fraction of a nanometer, capable of 3-dimensional imaging, sample manipulation and interaction force measurement (55, 56).

As observed in Figure 14, the AFM system consists on a sharp tip mounted on a micro-machined cantilever probe, connected to a Piezoelectric (PZT) actuator. Also, it includes a position sensitive quadrant photodiode (PSPD), responsible for detect a laser beam reflected of the back end-point of the tip, providing cantilever deflection feedback and position (z value) of the tip in relation to the surface (x and y value) (56).

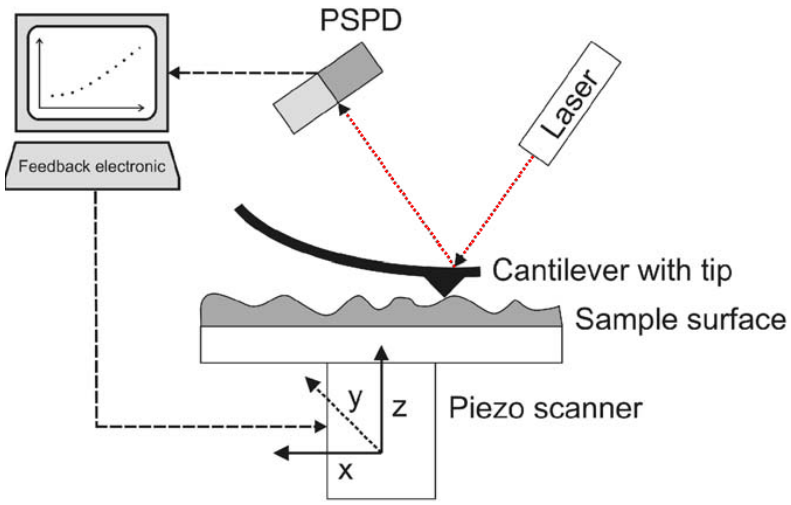

Figure 14 - Schematic illustration of an AFM equipment, figure adapted from (57).

The interaction forces between the tip and sample can be identified on a force–displacement curve, as show in Figure 15. When the distance between the tip and the sample's surface is large, weak attractive forces are generated. When the tip is brought closer, attractive forces increase until the electron clouds begin to repel electrostatically each other. These repulsive forces between the atoms provoke the weakness of the attractive forces, becoming zero when the distance between the atoms reaches a couple of angstroms and turning fully repulsive when the tip's atoms are in contact with the sample's surface (56).

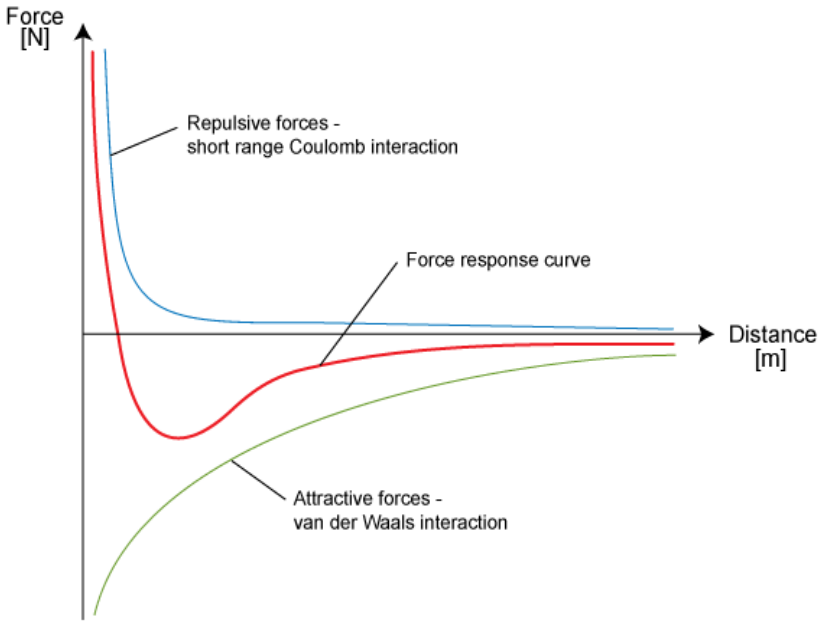

Figure 15 – Different force levels between the tip and the sample's surface with respect to the z-axis distance, figure adapted from (58).

Taking advantage of the forces of repulsion and attraction, AFM can operate in two main modes: in contact mode in the repulsive region and in non-contact mode in the attractive region (Figure 16).

In the contact mode (Figure 16), the tip is maintained in direct contact with the sample while it scans the surface, making the interaction forces with the tip and the surface repulsive in nature (i.e. van der Waals force dominates any other attractive force that may tend to act at this point) with a repulsive force of 10^{-8} N to 10^{-6} N. The topography surface is continuously analyzed by the constant contact of the tip with the surface, being very sensitive to slight variations in the surface. However, the main drawback of the contact mode is that the shear forces resulting from the movement of the tip in the sample tend to damage soft samples and distort the features of the generated image. Therefore, this mode is not suitable for analyze soft biological and polymer surfaces such as the DD films (56).

In the non-contact mode, the tip does not touch the surface, hovering about 50-150 Å above the sample surface, with a van der Waals attractive force of 10^{-12} N. In order to compensate the weaker attractive forces, the tip is given a small oscillation (Figure 16), so that these small forces can be detected by measuring the variation in amplitude, frequency, phase of the oscillating cantilever (56). For this mode, it is very important to keep the surface in the higher aseptic state possible, to avoid image distortion. In this work, the non-contact mode was used to analyze de DD films, once, unlike the contact method, it does not alter the morphology or damage polymer surfaces.

In addition, this non-contact mode allows the use of phase-constant imaging, which is a

powerful tool that creates surface images with greater detail, not achievable with normal topographic imaging. This is achieved by comparing the cantilever oscillatory phases (i.e. affected by viscosity, friction, etc.) with the AFM standard frequency, being especially important in samples that present different materials with different types of viscosity (59).

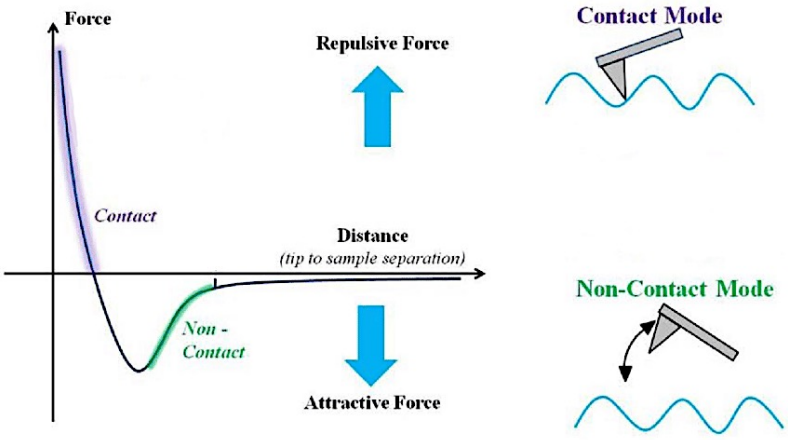

Figure 16 - different types of contact with different means of force interaction, figure adapted from (60)

In this work, phase contrast imaging was used to determine changes in composition of each layer of the DD film (56, 59). By color-mapping each individual value of z with the corresponding x and y position, the AFM software was able to create a topographic image, used to analyze and compare changes in the layers after adsorption. These images were then further optimized. All measurements were performed in non-contact mode using silicon tips, with 256x256 pixels resolution and a scanned area of 2x2 μm^2 and 10x10 μm^2 (the 10x10 μm^2 topographic images are in Appendix).

The Nano-Observer AFM from CSInstruments was used in all the experiments, in the Organic Electronics group at Instituto de Telecomunicações as show in the Figure 17.

Figure 17 – the Nano-Observer AFM used to analyse the layer of the DD films.

In order to characterize the samples surface, the Root-mean-square (Rrms) was used to quantify spatial differences in each monolayer where N is the number of lines and de M the number of columns. The analyzed surfaces were characterized through the calculation of the height distributions of the gains (z (x,y) value), using the formula below:

$$\mathrm{Rrms}(N,M) = \sqrt{\frac{1}{NM}\sum_{x=1}^{N}\sum_{y=1}^{M}[z(x,y) - z_{med}(N,M)]^2} \qquad \textbf{Equation (4)}$$

2.2.4 Neutron reflectivity

The neutron reflectivity (NR) is a non-destructive technique that allows the analysis of thin layers thickness with a resolution ranging from 5 to 50000 Å (61). The specular reflection measurement principle consists in determining the coefficient of reflection of a neutron beam sent diagonally to a sample, and by analyzing the density profile of the neutron scattering length perpendicular to the plane of a surface or interface, allows the chemical composition and thickness to be determined (62). The Figure 18 shows a simplified scheme of the NR technique, as well as the common obtained results.

In a simplified way, the values obtained during the measurement are processed by the computer through advanced mathematical formulas (Figure 18 - a)), originating from there an interpolated point graph (Figure 18 - b)), which in turn is model fitted to the sample measurements (Figure 18 - c)).

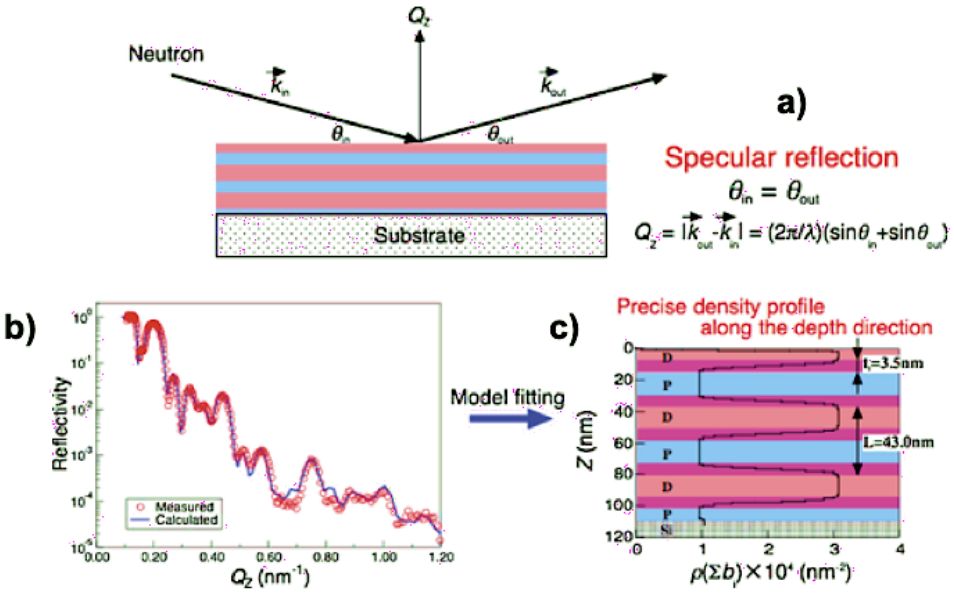

Figure 18 - Simplified scheme of a neutron reflectivity instrument and results, here: K_{in}=incoming beam; K_{out}= outgoing beam; Q_z= surface normal; θ_{in} = incident angle and θ_{out}=reflected angle. Figure adapted from (63)

In the NR technique, the minimum reflectivity value used experimentally directly influences the thickness value that can be observed. Such minimal reflectivity value is usually between 10^{-6} and 10^{-7} in samples with only a few cm^2. There are other laboratory instruments, such as X-Ray reflectivity, that have lower minimum reflectivity values than NR. Therefore, this instruments are preferable in many experimental cases, being used as a complementary measurement to NR, as it provides information on the electron density profile (62).

However, neutrons have some unique advantages in comparison to photons, that makes them capable of measurements that are impossible to obtain using the X-Ray reflectivity for example, the characterization of buried interfaces in soft matter, among others. This is due to the fact that the interaction occurs directly between the neutron and the nuclei of atoms and not with the electronic cloud, as in the case of X-rays. This difference comes from the fact that neutron reflection index is very dependent of its content on hydrogen atoms, and by replacing the hydrogen atoms of a molecule by deuterium atoms, it will strongly modify its refraction index without alternating significantly its physical and chemical form. This allows to tune the neutron refractive index, for example, by labeling some molecules with deuterium, which will increase the contrast in the system, and by mixing hydrogenated and deuterated solvents in order to match one of the layers in the system, will make it invisible from the neutron point of view (62). This was successfully applied the field of polymers (64).

NR technique is able to study deeper layers also because, contrarily to X-Ray reflectivity, neutrons are barely absorbed by matter, except for a few atoms that have a huge neutron absorption, such as boron, gadolinium, lithium. This weak interaction allows to analyze the buried interfaces and to study *in situ* experiments in various sample environments.

NR is also ideal for non-destructive analysis, once the neutrons wavelengths used in experiences are typically in the range of 1 to 20 Å and have an energy of a few meV. Contrarily to X-rays, that uses wavelengths with energy in the order of keV (62), ideal for biological materials, such as the multilayer films.

The NR measurements were made at the Laboratoire Léon Brillouin in France (65) under the european funding NFFA.EUROPE.

2.2.5 Drug delivery layer-by-layer films preparation

All laboratory glassware used to prepare the films were previously cleaned with “piranha solution”, which consist in a mixture of H_2SO_4 and H_2O_2 (2:1) during about 45 minutes to remove any organic substances followed by a washing with distilled and milli-Q water. The films were made on the top of quartz substrates that were also washed using the same procedure described above. After washing, a 10 minutes of oxygen plasma in the vacuum chamber Plasma Prep 2 from Gala Instrument was perform, increasing the hydrophilicity of the substrate surface improving the adsorption of the first polymer.

In this work, each bilayer was formed using the four steps of LbL technique schematized in the Figure 19. The adsorption times of each layer were previously optimized in order to ensures the formation of each layer. First, the hydrophilic substrate was immersed into a PBAE solution, during approximately 6 minutes. After this, the substrate was remove from PBAE solution and dipped in sodium acetate (pH= 5.0) three times, to remove all molecules that were not adsorbed or only partially adsorbed to the surface. After these two steps, a PBAE monolayer is formed. Then, the formed monolayer was immersed into the (Poly-CD+Brim) solution, for 11 minutes, following by the dipping in a new sodium acetate solution (pH= 5.0) three times and the drying with nitrogen gas. After these two final steps, a monolayer of (Poly-CD+Brim) is formed on top of the PBAE monolayer, creating one (PBAE/Poly-CD+Brim) bilayer, completing one cycle of the LBL assembly. This newly created bilayer was measured directly on the substrate inside the UV-vis spectrometer, ensuring the correct formation of the new bilayer on the subtract surface.

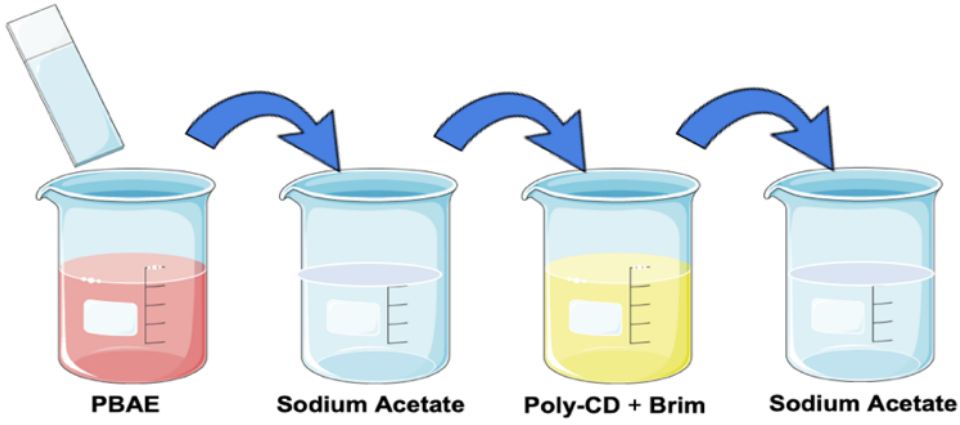

Figure 19 – Schematic representation of the LbL technique used.

This cycle was repeated, forming DD films with six as a maximum number of bilayers per substrate. After the LbL assembly, the resulting film constituted by $(PBAE/Poly\text{-}CD+Brim)_6$ should resemble the scheme in Figure 20.

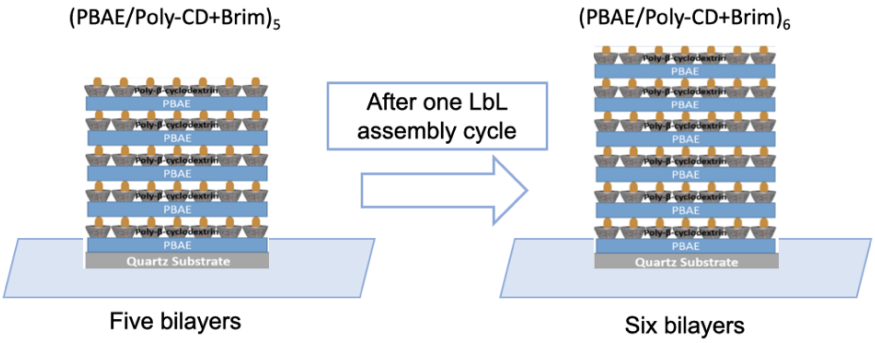

Figure 20 –Schematic representation of a LbL assembly with (PBAE/Poly-CD+Brim) bilayer, figure adapted from (66).

2.2.6 3D printing

The term “3D printing” describes the process to create a three-dimensional model under computer control, through the fusion and solidification of a suitable material. (67) Also known as layered manufacturing or additive manufacturing, this process is based in an object built from a computer-based design (CAD) by successively adding material layer by layer. (68)

There are several techniques of 3D printing and generally they use an extrusion process called fused deposition modelling (FDM). This technique utilizes the additive approach, in which a continuous thermoplastic filament is heated to a semi-molten state before extrusion for layer-by-layer deposition. (69) Figure 21 shows the schematic representation of this technique.

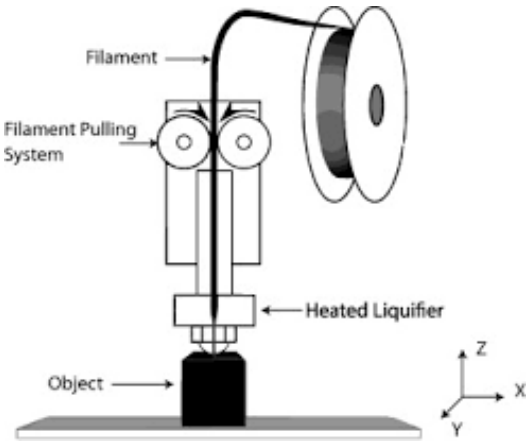

Figure 21- simplified representation of the operation of the FDM technique, figure adapted from (70).

The first step of printing a 3D object is to create a CAD model to a Standard Triangle Language (STL) file format, which stores information on the 3D object coordinates and surfaces. After that, a specialized slicing program divides the 3D model into several 2D cross-

section layers and sends the information to the 3D printer to process. (71)

Finally, the 3D printer's extruder head is fed with a filament from a large coil (Figure 21) and moves under the computer's control coordinates forming a layer in two dimensions (X and Y axle), depositing the heated filament onto the print bed. After the conclusion of the first layer, the print head is then slightly moved vertically (Z axle) to begin a new layer and this process is repeated until the entire 3D object is completed. (70, 72)

The 3D printer used for this work was a HelloBeePrusa by BeeVeryCreative in the Chemistry laboratory at Instituto Superior de Engenharia de Lisboa (ISEL) (Figure 22 – e)).

All parts of the 3D printer were manually assembled (Figure 22 – a) to d)) and it had calibrated before the object could be printed. Its main objective was to print the dynamic cells sliced by Ultimaker Cura® and created in CAD using Autodeck® Tikercad™ program (73).

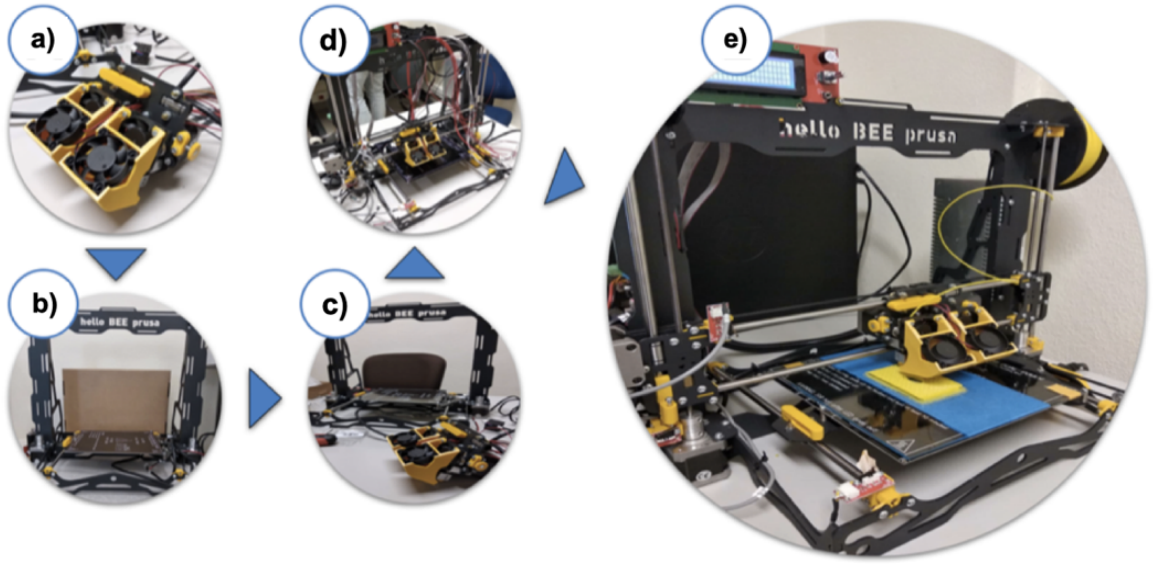

Figure 22 - Schematic image of HelloBeePrusa's construction; a) - complete assembly of extruder module; b) - complete assembly of support structure; c) – connection of support structure with extruder head; d) - assembly of electronic component; e) - assembly completed and operational.

2.2.7 Dynamic cell designs

The dynamic cell design went through various stages of evolution until the desired cell design was obtained. The first one was based in cell to be inserted inside of the UV-Vis spectrophometer in order to evaluate the drug release kinetic in real time. Figure 23 shows the setup that was developed which consisted in a transparent plastic cell to follow the solution that continuously passes inside. This cell was not printed but it was fabricated from three plastic cells glued together. To test the cell, preliminary tests were performed using a

solution of $K_2Cr_2O_7$ with a concentration of 78mg/L that was inserted in the burette, dropping one drop of solution approximately every 2 seconds, into the cell.

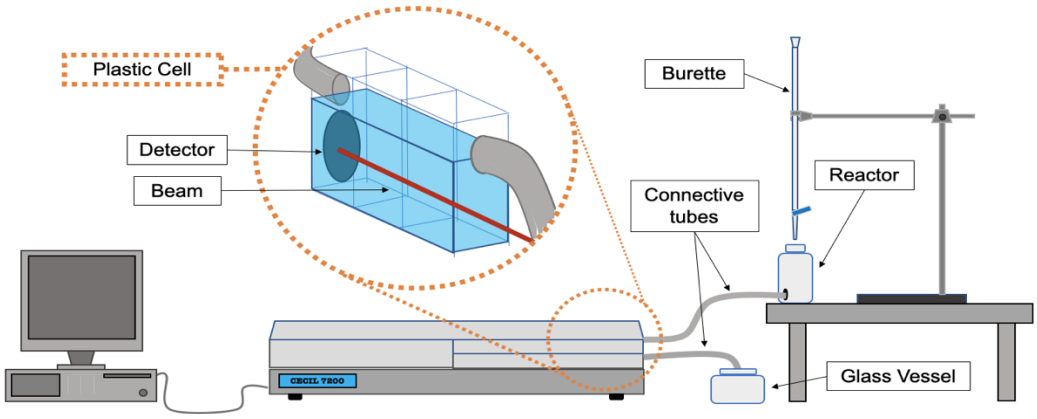

Figure 23 –Scheme illustrating the assembly used to test the variation of concentration of $K_2Cr_2O_7$, in relation to time.

With the first drop falling into the cell, the first spectrum was performed, obtaining new spectra measurement every 2 minutes. The test was finished when all the content of the 50 mL counter ended. The results are shown in Figure 24.

In Figure 24, a zoom in graph between 290 nm and 340 nm wavelengths can be seen, showing a progressive increase in $K_2CR_2O_7$ absorbance was the time advances, validating the theory that it is possible to track the change in absorbance *in-situ* in UV-vis inside the spectrophotometer.

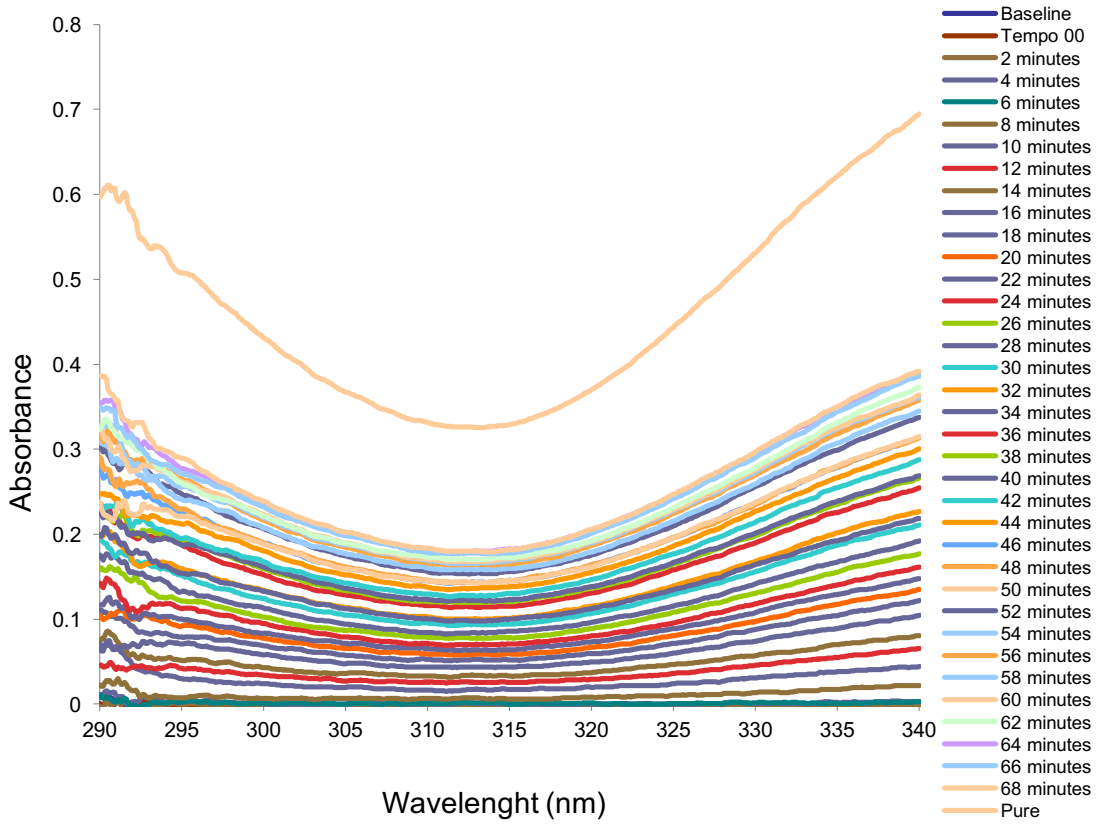

Figure 24 *– Zoom in graph between the 290 nm and 340 nm, showing the variation of the absorbance of $K_2Cr_2O_7$ values within the cell, in relation to time (measured every to 2 minute).*

Using the absorbance peak of 313 nm, a correction graph between the absorbance and time was created in order to show that the absorbance value increased linearly over time, as can be seen in Figure 25.

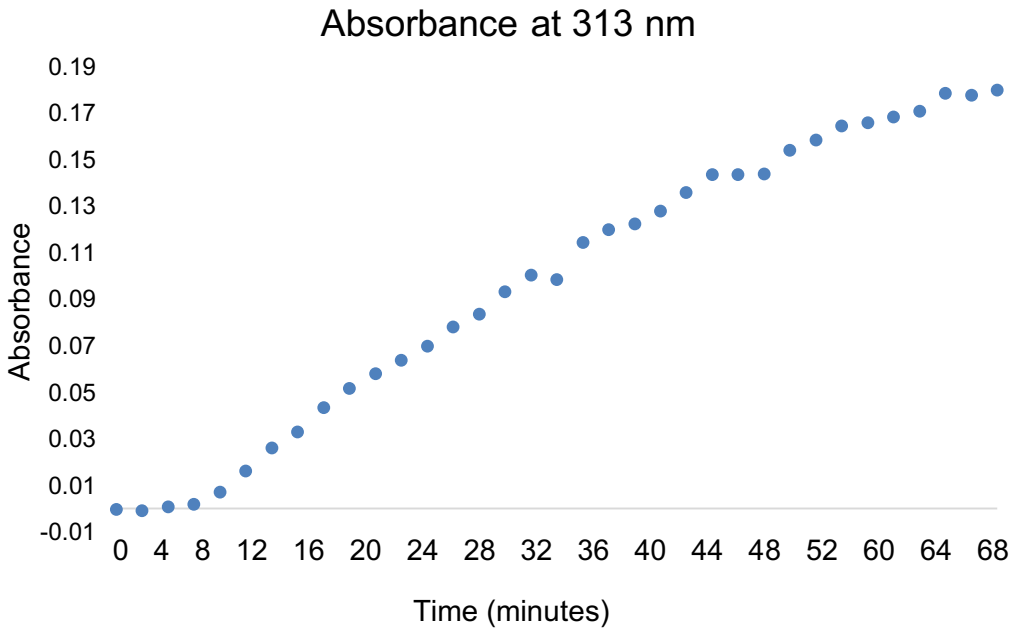

Figure 25 – Absorbance of $K_2Cr_2O_7$ at 313 nm, in relation to time.

Observing the graph above, that as $K_2Cr_2O_7$ is released to the cell, it increases its concentration within the dynamic cell in a progressive and linear fashion over time.

To determine if the implementation of a stirring motor inside the UV-vis measuring chamber could affect the spectra, a control test was performed. Using three different types of stirring motors (motor A, B and C) placed directly in the spectrophotometric measuring chamber, $K_2Cr_2O_7$ spectra were obtained (Figure 26).

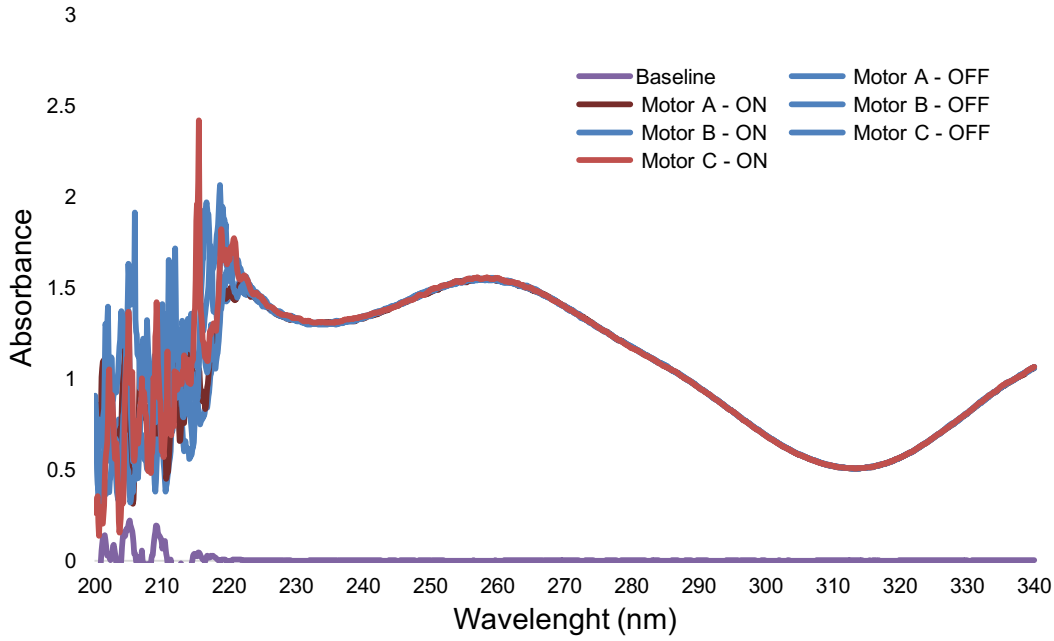

Figure 26 - Absorbance spectrum of motor A, motor B and C.

The first measurement was made without any motor in the chamber to create the reference, followed by two measurements with the motor A inside, one made with the motor switch “OFF”, and another with the motor switch “ON”, respectively. This process was repeated in the same way for motor B and C. The results from the motor switch “OFF” and “ON” are show in the Figure 26, with a zoom in graph between 240 nm and 280 nm zone in Figure 27.

After analyzing the dada in Figure 27, it is possible to visualize that the spectra obtained are practically identical over the entire wavelength in all motors, overlapping almost completely. Concluding that there are no significant differences between any of the motors, whether being “ON” or “OFF”.

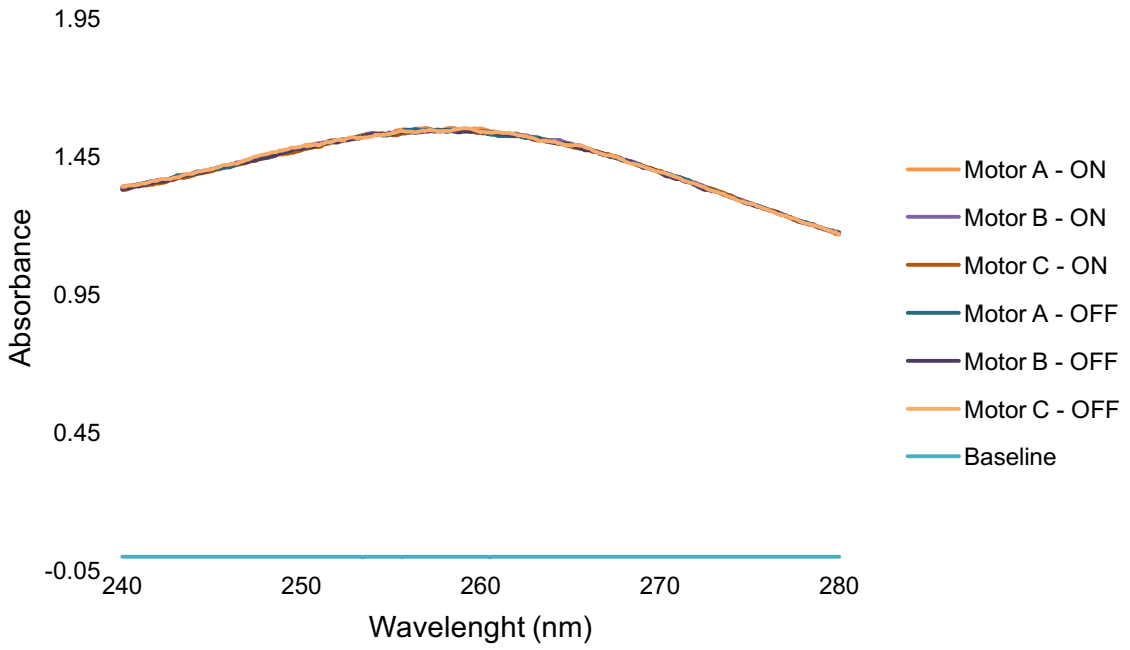

Figure 27 - Absorbance spectrum of motor A, motor B and C (zoom in graph between 240 and 280 nm of Figure 26).

In conclusion, through these preliminary tests, it was possible to verify the ability of the spectrophotometer to detect small absorbance variations inside a cell with dynamic behavior in real-time, obtaining a constant increase in the absorbance over time without any interference from the stirring motors, as theoretically intended.

After these tests, dynamic cells were 3D printed using a yellow PLA filament at temperature of 215 ºC and a print resolution of 0.2 mm.

For the design of the dynamic cell, several measurements and anatomic factors of the ocular system were taken into consideration, being the surface area, the volume of the tear film and the speed of renewal the most studied. In order to determine the flow rate to be used in the experiment, calculations were made to find out the percentage of tear renovation that occurred per minute on the ocular surface. This way, the surface area of the eyeball was calculated to determine the total tear film volume.

Given the anatomical differences of each individual, an exact value of the surface area of the globe could not be determined, so an average value of 18.10 cm^2 of the values found in the literature was used (74, 75). Of this total area, only the anterior part of the globe is covered by tear film, which corresponds to approximately 1/3 of the superficial area of the ocular globe, which means approximately 6 cm^2.

The tear film is comprised of 3 layers, a 0.1 to 0.2 μm thick lipid layer, a 6 to 10 μm thick aqueous layer, and a 0.03 μm thick mucus layer. However, depending on the author, its total thickness may vary from 6 μm - 20 μm (76, 77). Considering the discrepancies in the tear thickness values, an intermediate value of 10 μm thickness was considered for these calculations. Considering the values presented above, the average volume of the tear film at a given moment is given by:

$$\text{Tear Film Volume} = 6\ \text{cm}^2 \times 10\ \mu\text{m} = 7.2 \times 10^{-3}\ \text{cm}^3 \qquad \textbf{Equation (5)}$$

Several studies have determined that the rate of tear renewal is approximately 1.2 μL/min or 1.2 x10^{-3} cm^3/min (78, 79). Using this value, the renewal percentage rate (RPR) is given by:

$$RPR = \frac{1.2 \times 10^{-3}\ cm^3}{7.2\ \text{x}10^{-3} cm^3} \times 100\% = 16.7\% \qquad \textbf{Equation (6)}$$

These values were considered as the starting point for the dynamic kinetics, allowing to correlate the tear film renewal rate with the cell flow rate in relation to its volume and mimetizing the anatomical behavior.

Using the Autodeck® Tikercad™ program (73), the first printed cell design was created. This prototype consisted in a basic rectangular cell with two circular openings, where 2 silicone tubes were fitted and through which the liquid would pass, as shown Figure 28. More dimensions of the cell design can be seen in Figure 48 in Appendix

The cell had an internal volume of 44.16 cm^3 and it was used to evaluate the dynamics of the aqueous solution. Despite it had the overall shape of the desired cell, when the placing the film inside the cell, the lack of agitation led to low homogeneity of the medium. However, when an agitator was placed along with the film in the medium, the agitation caused an abrupt rupture of the layers out of the substrate, and thus, completely destroying it. Another problem was the absence of a film attachment point, causing the film to not remain firmly fixed upright inside de cell and at risk of falling during adsorption. So, in order to properly accommodate the multilayer film substrate and a magnetic stirrer inside the cell, some changes were required.

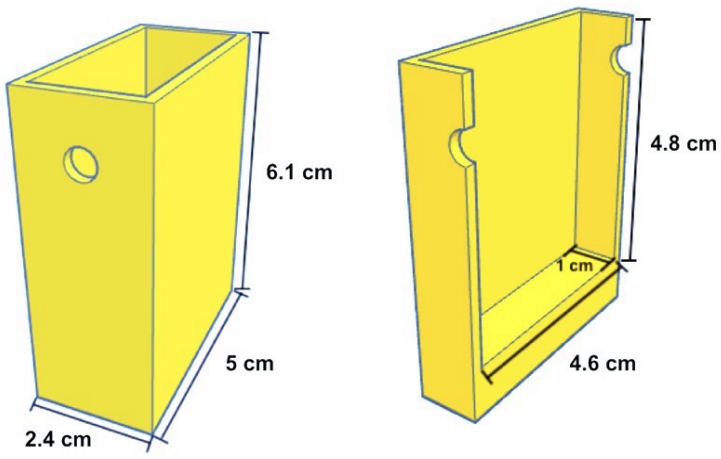

Figure 28 – Schematic representation of the outer part of the 1ª prototype cell (left figure) and the inner part (right figure).

To make the prototype cell compatible with the magnetic stir bar, an accessory chamber with approximately 2.288 cm^3 and a 1 cm thick barrier was design, with the function of isolate the dynamic cell from the turbulence generated by the stir bar, as can be observed in Figure 29. The remaining cell's dimensions can be seen in Figure 49 in Appendix

The addition of a slot in the lower cell surface was another required improvement (Figure 29) to fix the Brimonidine film vertically, allowing the flow of PBS through both sides of the substrate. After all these changes, the cell had a total final volume of 35.08 cm^3.

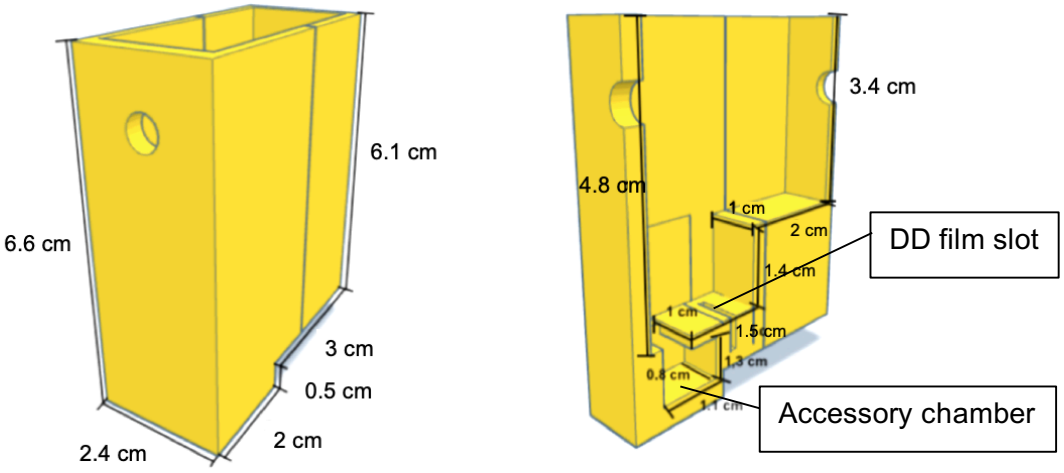

Figure 29 –Schematic representation of the outer part of the 2º prototype cell (left figure) and the inner part (right figure), with accessory camera and DD film slot included.

The next step was to develop an attachment for the cell, in order to fit in the bracket fitting of the UV-Vis spectrophotometer, allowing for the absorption measurements to be taken directly inside the spectrophotometer, without having to remove the samples. For this, a CAD copy of the original spectrophotometer docking bracket was developed and later added to

the side of the dynamic cell, allowing the cell to stay attached to equipment, as shown in the Figure 30 below. More docking bracket and cell design measurements can be seen in Figure 50 and Figure 51 in Appendix.

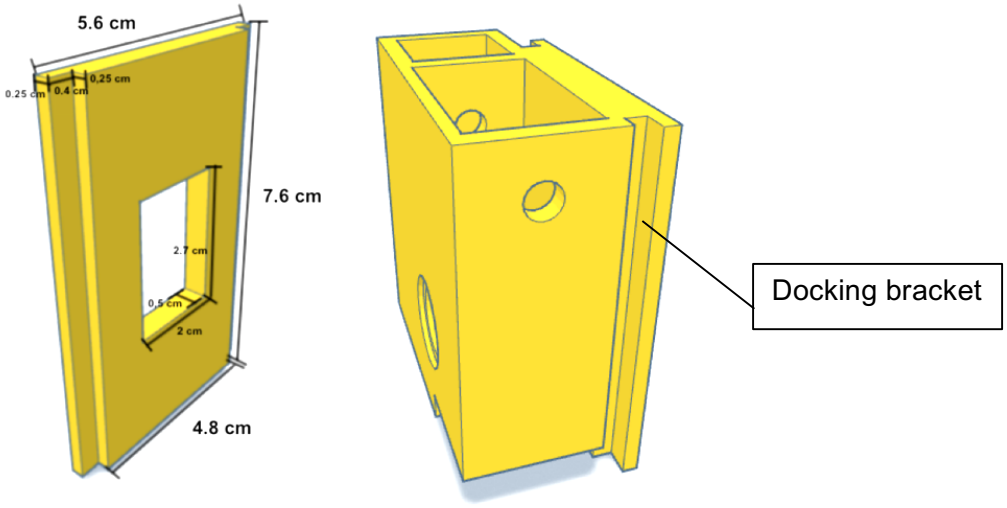

Figure 30 - Schematic representation of the UV-Vis spectrophotometer docking bracket (left figure) and outer part of the 3º prototype cell (right figure) with embedded quartz window and docking bracket already added.

In addition to the support, another fundamental change to obtain the absorption spectra directly, was the creation of a quartz window with 1.3 cm diameter on both sides of the cell, allowing the UV-Vis beam to pass through, as can be seen in Figure 31.

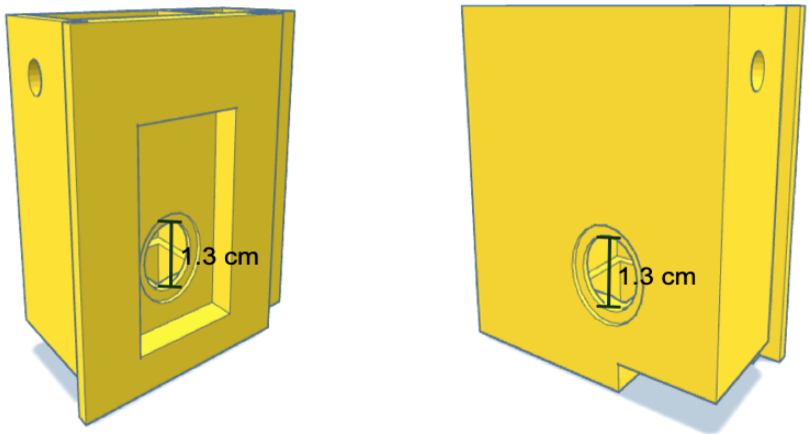

Figure 31 – Schematic representation of the 3º prototype cell embedded quartz windows.

Lastly, a runoff camera was added to the dynamic cell to improve the flow of the liquid existing in the reaction chamber, eliminating the occurrence of resistance to liquid exit from the reaction zone (Figure 32). The final internal volume of this cell was 33.923 cm^3, plus the runoff camera with 17.75 cm^3.

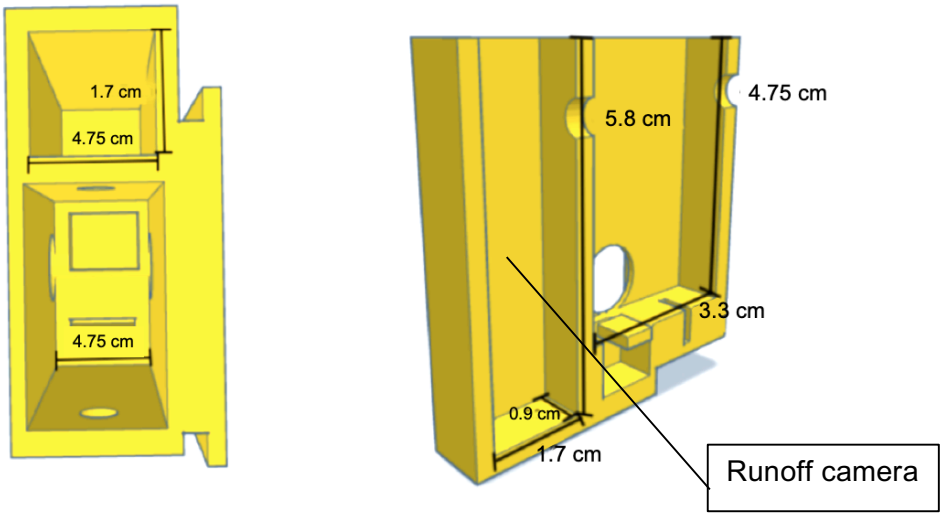

Figure 32 - Schematic representation of the 3º prototype cell seen from above (left side) and the inner part (right side) with the runoff camera added to the cell.

However, when testing the kinetic with the DD film inside, contrary to what was predicted by the preliminary in-situ tests (Figure 24), high interferences in the final spectrum did not allow conclusive values on the kinetics of the film.

The most probable cause for such interferences may duo to the fact that small quartz windows were used and glued with epoxide resin. These two factors may have led to interference in the UV-Vis spectra, since glue residues may have easily stayed on the center of the quartz window and intersected the UV-Vis beam. One example of a spectra affected by interference of the quartz windows can be seen in Figure 33 below.

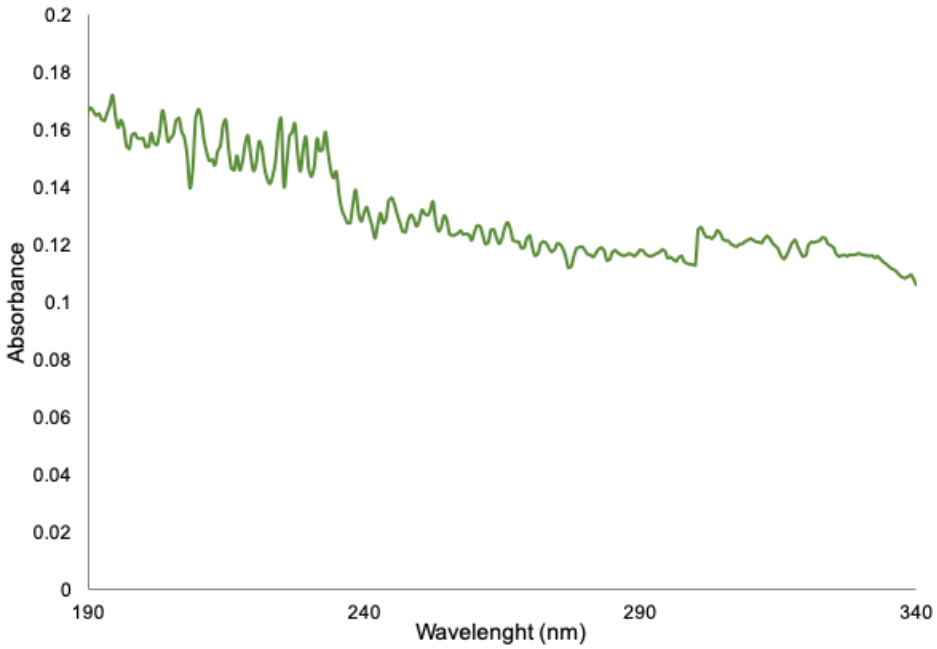

Figure 33 – sample spectra graph with interference caused by unknown factors inside the dynamic 3D cell placed on to the UV-Vis Spectroscopy

Due to these high interferences, this design was considered not suitable for this work and an alternative cell was fabricated to follow the drug release kinetic outside the UV-Vis spectrophotometer. The final design is presented in Figure 34 (Figure 52 in Appendix) and it was used to obtain all kinetics results presented in Chapter 4.

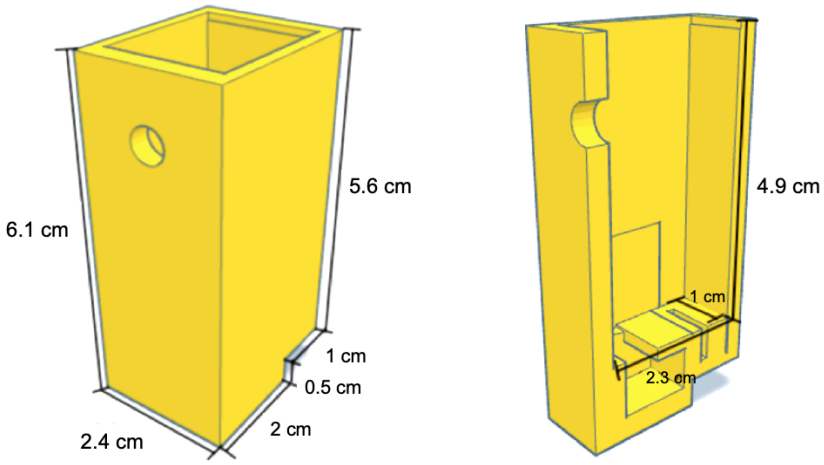

Figure 34 – Schematic representation of the final cell used for kinetics, dynamics from outside (left side) and inside (right side) with accessory camera and slot added.

This dynamic cell was developed to have the smallest possible reaction chamber volume. The cell has a volume of 22.54 cm^3 for the reactive chamber, plus a shaking chamber of 2.288 cm^3, giving a total of 24.82 cm^3. In this drawing, the cell has only one flow hole, since the aim would be to use a burette on top of the cell, dropping into the upper aperture. In order to simulate the ocular environment, the flow rate had to be determined, using the previously calculated RPR value of 16.7%, we can determine the appropriate flow rate for this dynamic cell that is given by:

$$\text{Flow Rate} = 24.82\text{cm}^3 \times 16.7\% = \ 4.14\ \text{mL/ min} \approx 4\ \text{mL/min} \qquad \textbf{Equation (7)}$$

Reynolds coefficient (Re) was also calculated to determine if the flow within the 0.2 cm diameter tubes was either laminar or turbulent, given by:

$$\text{Re} = \frac{\rho \times \nu \times D}{\mu} \qquad \textbf{Equation (8)}$$

Being that the ρ is the specific mass of the fluid, ν the average fluid velocity, D the pipe diameter and μ the dynamic fluid viscosity. For this calculation, water's specific mass and dynamic fluid viscosity were used ($\rho = 1000\ \text{kg/m}^3$ and $\mu = 1.003\times10^{-3}\ \text{Pas.s}$) (80)

Using the flow rate and volume values given above, the calculated velocity for the tube was: $\nu = 0.0219\ \text{m/s}$. By applying the Reynolds coefficient formula:

$$\text{Re} = \frac{1000\ \text{kg}/m^3 \times 0.0219\ \text{m/s} \times 0.002\ \text{m}}{1.003\times10^{-3} Pas.s} = 43.67 \qquad \textbf{Equation (9)}$$

The result given by the Reynold coefficient formula is dimensionless and it considered that the flow is laminar regime, in the case of water flow in a cylindrical pipe with values below 2000. (80) Since the value obtained was 43.67, the flow rate within the tube is laminar.

2.2.8 Dynamic cell setup

The final setup for the kinetics tests is shown schematically in Figure 35. The solution to be analyzed is added to the burette that is held by a universal support and it flows to the printed cell and then the solution is acquired in the glass vessel.

In order to determine how many drops per minute are equivalent to a flow rate of 4.14 mL/min, some calculations were performed, knowing that one drop is equivalent to approximately 0.05 mL (81), it was deduce that:

$$\frac{4.14\ \text{mL}}{0.05\ \text{mL}} \approx 83\ \text{drops} \qquad \textbf{Equation (10)}$$

From this calculation, we can conclude that 4.14 mL/min is approximately 83 drops/min. Using a stopwatch, the burette was previously calibrated, in order to drop 83 drops of PBS into the dynamic cell in one minute.

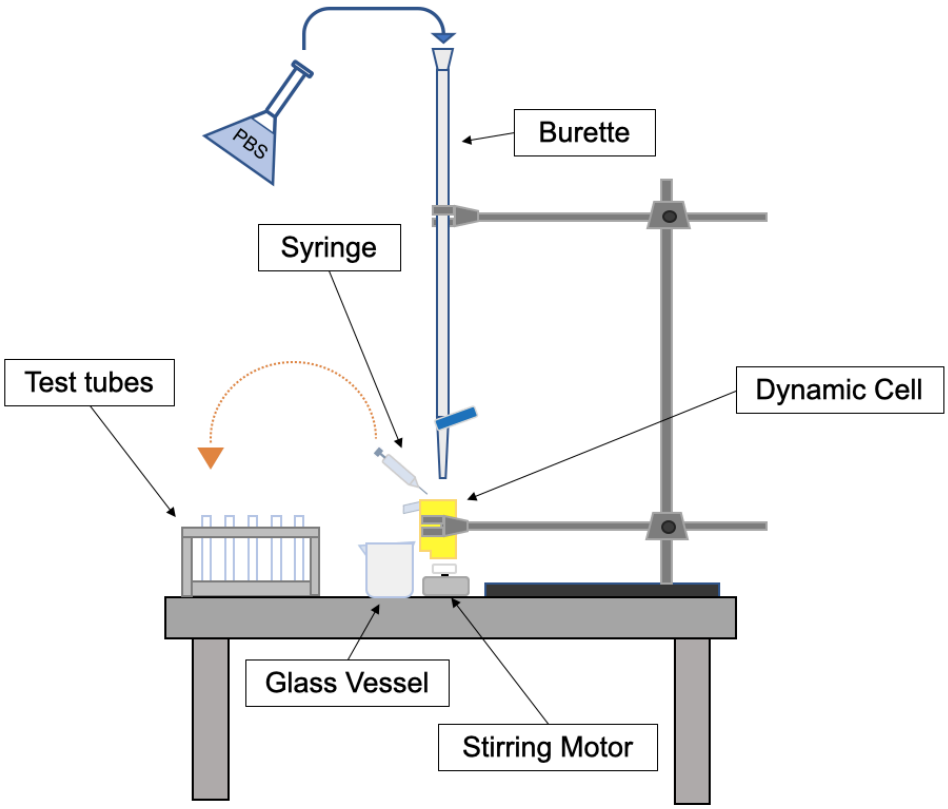

Figure 35 – Schematic representation of the setup used to perform the kinetics.

Inside the dynamic cell, a small agitator was placed into the accessory camera, above the stirring motor (Figure 35), allowing the homogenization of the solution.

After the system was in equilibrium and correctly calibrated, a 5 mL PBS sample was taken using a syringe and placed in a test tube. This sample was used as the reference for the UV-Vis spectroscopic analysis.

Using the stopwatch, the time was set to begin the experience when the DD film was placed into the cell's slot. Samples were taken in defined timings, which were: two samples with 5 mL during the first minute; one 5 mL sample every minute until the time of five minutes was reached; until the fifteen minutes, 5 mL samples were taken every two minutes; from the fifteen minutes mark to the final mark of two hours, 5 mL samples were taken every five minutes. A total of thirty-three samples were taken and placed in pre-labeled test tubes.

Chapter 3 – Drug Delivery: Films Growth

3 Drug Delivery: films growth

This chapter discusses the monitoring of DD film growth created by the LbL technique using UV-Vis spectroscopy, AFM and NR. The UV-Vis spectroscopy was performed after each new bilayer formation on the film. The AFM technique was used to analyzed each bilayer's morphology and the NR to analyze the thickness of each layer.

3.1 UV-Vis spectroscopy analysis

The LbL films growth was studied using UV-Vis spectroscopy in order to monitor the (PBAE/Poly-CD+Brim) bilayer formation step-by-step. After the creation of a new bilayer, the substrate was placed into the UV-Vis spectrometer and a new absorption spectrum was recorded.

During the analysis, a sequential increase in the intensity of each spectrum corresponding to a new bilayer is expected, confirming the formation of a new bilayer. If the spectrum obtained overlapping the previous layer's spectrum, the new bilayer was not completely formed. In this case, the substrate was immersed again in the (Poly-CD+Brim) solution and washed in the sodium acetate solution in a new attempt to completely create a new bilayer. The new bilayer formation was again confirmed in the spectrophotometer. In the cases that bilayer formation was not well succeeded, the process was repeated only one more time. When a complete bilayer was formed and confirmed in the spectrophotometer, the process continued to the next bilayer.

The UV-Vis spectroscopy monitoring results of the multilayer films growth as shown in Figure 36. Each spectrum was obtained after the creation of a new bilayer and each one of them presented a higher intensity than the previous one, indicating that the bilayer deposition was well succeeded (for the remaining LbL growth monitoring graphs – see Appendix). Three films were made in order to evaluate the reproducibility and they are represented in Figure 53, Figure 54 and Figure 55 in the Appendix.

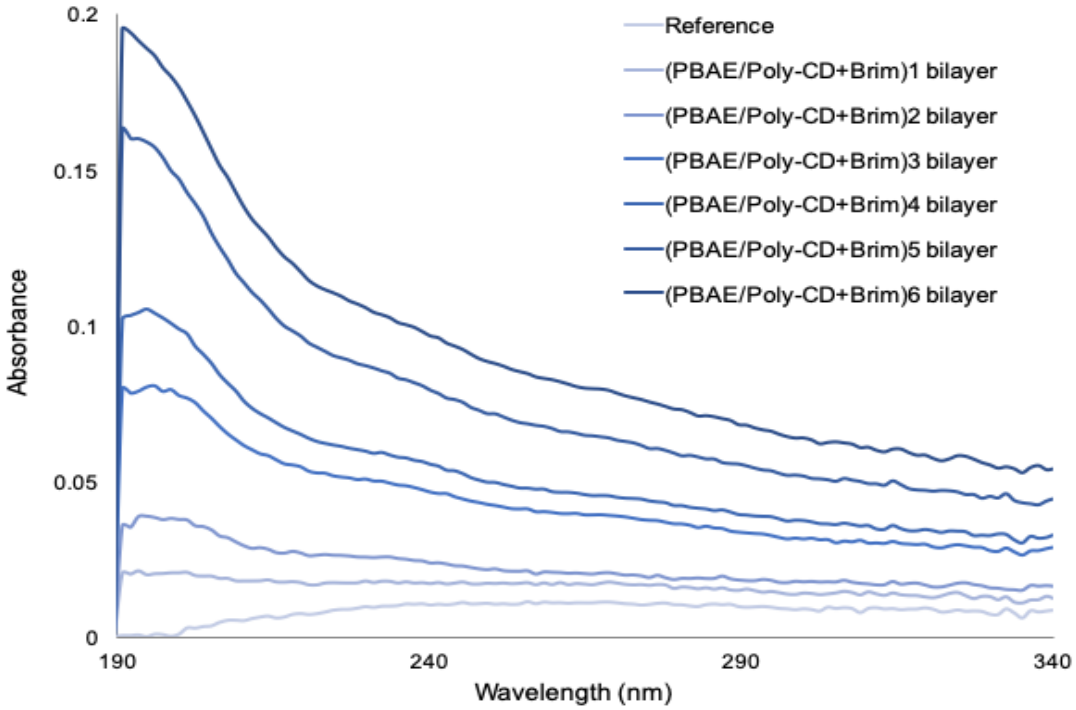

Figure 36 - Absorption spectra of six (PBAE/Poly-CD+Brim) bilayer of the 1st LbL Film, obtained after each bilayer deposition.

Observing the presented spectra, the first spectrum represents the reference, consisting only by the quartz substrate. The second spectrum, which was a higher intensity when compared to the reference spectrum, corresponds to the first bilayer (Figure 36 - (PBAE/Poly-CD+Brim)1) and the third spectrum corresponds to the second formed bilayer (Figure 36 - (PBAE/Poly-CD+Brim)2). An intensity increase is present in relation to the previous spectrum, due to the presence of two bilayers on top of the substrate instead of just one bilayer. This repeated behavior happens after each LbL technique cycle, increasing the intensity as the number of bilayer deposited on the substance increases. Despite the abundance increasing as each layer was deposited, the ΔAbsorbance was not constant, as can be observed in the figure 37

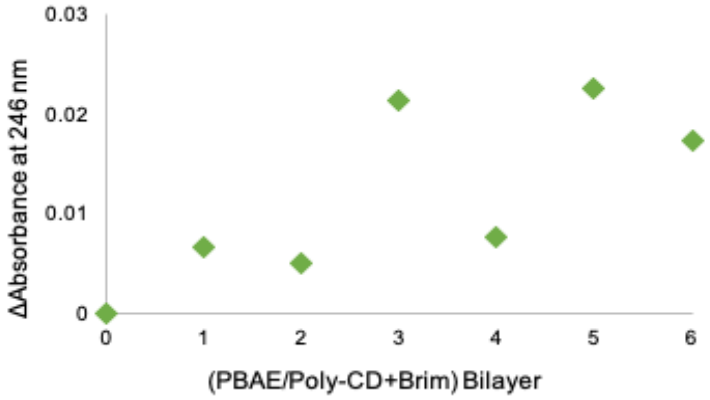

Figure 37 – Absorbance variation of the six (PBAE/Poly-CD+Brim) bilayer of the 1st LbL Film, obtained after each bilayer deposition.

3.2 Atomic Force Microscopy analysis

To characterize the surface of each formed bilayer, six mica substrates with six different number of bilayers were developed and analyzed by AFM, in order to obtain the morphology and roughness of each bilayer. The composition of the films that were analyzed are schematized in Figure 38.

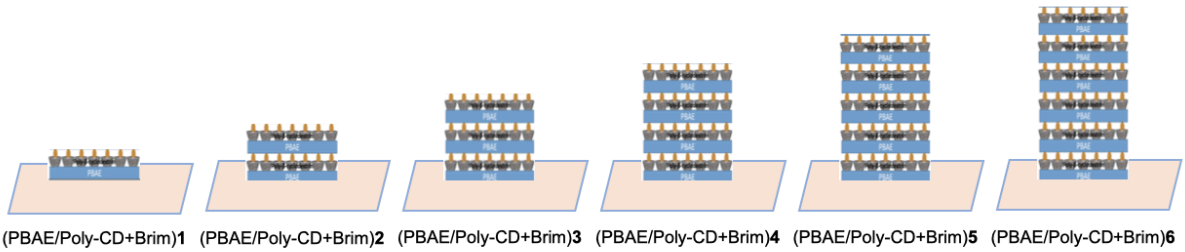

Figure 38 - Schematic representation of the (PBAE/Poly-CD+Brim) bilayers created in mica substrates using the layer-by-layer technique.

All films presented the same (PBAE/Poly-CD+Brim) bilayer configuration, varying only in the number of layers added on the top of each mica substrate. As shown in Table 2, AFM's phase image was applied together with the topography image during the scanning, allowing the characterization and comparison of the first $(PBAE/Poly\text{-}CD+Brim)_1$ film surface with the second $(PBAE/Poly\text{-}CD+Bim)_2$ film surface and so on. A line profile analysis was also determined in order to analyze the roughness of each bilayer film.

Table 2 – AFM images of LbL films composed of: a) $(PBAE/Poly\text{-}CD+Brim)_1$; b) $(PBAE/Poly\text{-}CD+Brim)_2$; c) $(PBAE/Poly\text{-}CD+Brim)_3$; d) $(PBAE/Poly\text{-}CD+Brim)_4$; e) $(PBAE/Poly\text{-}CD+Brim)_5$ and f) $(PBAE/Poly\text{-}CD+Brim)_6$.

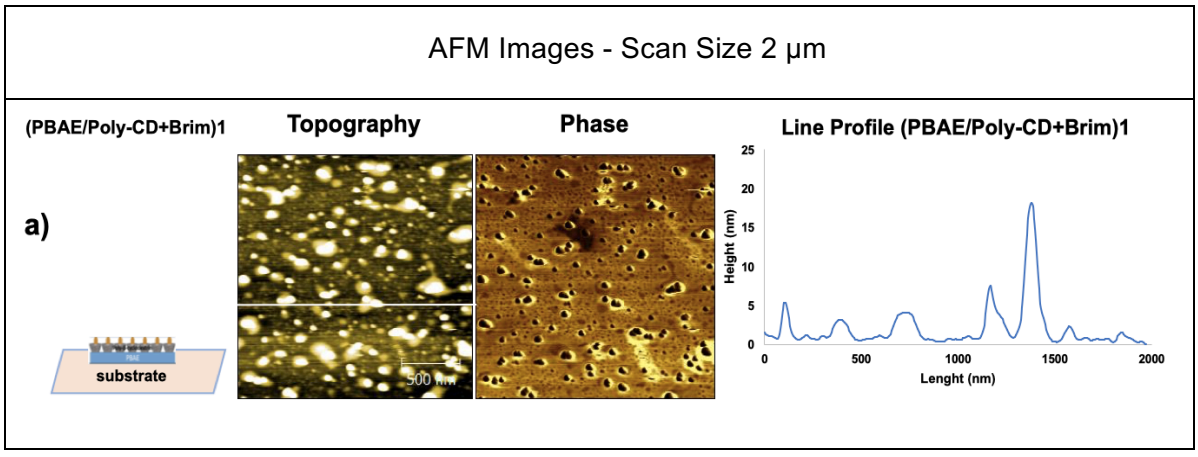

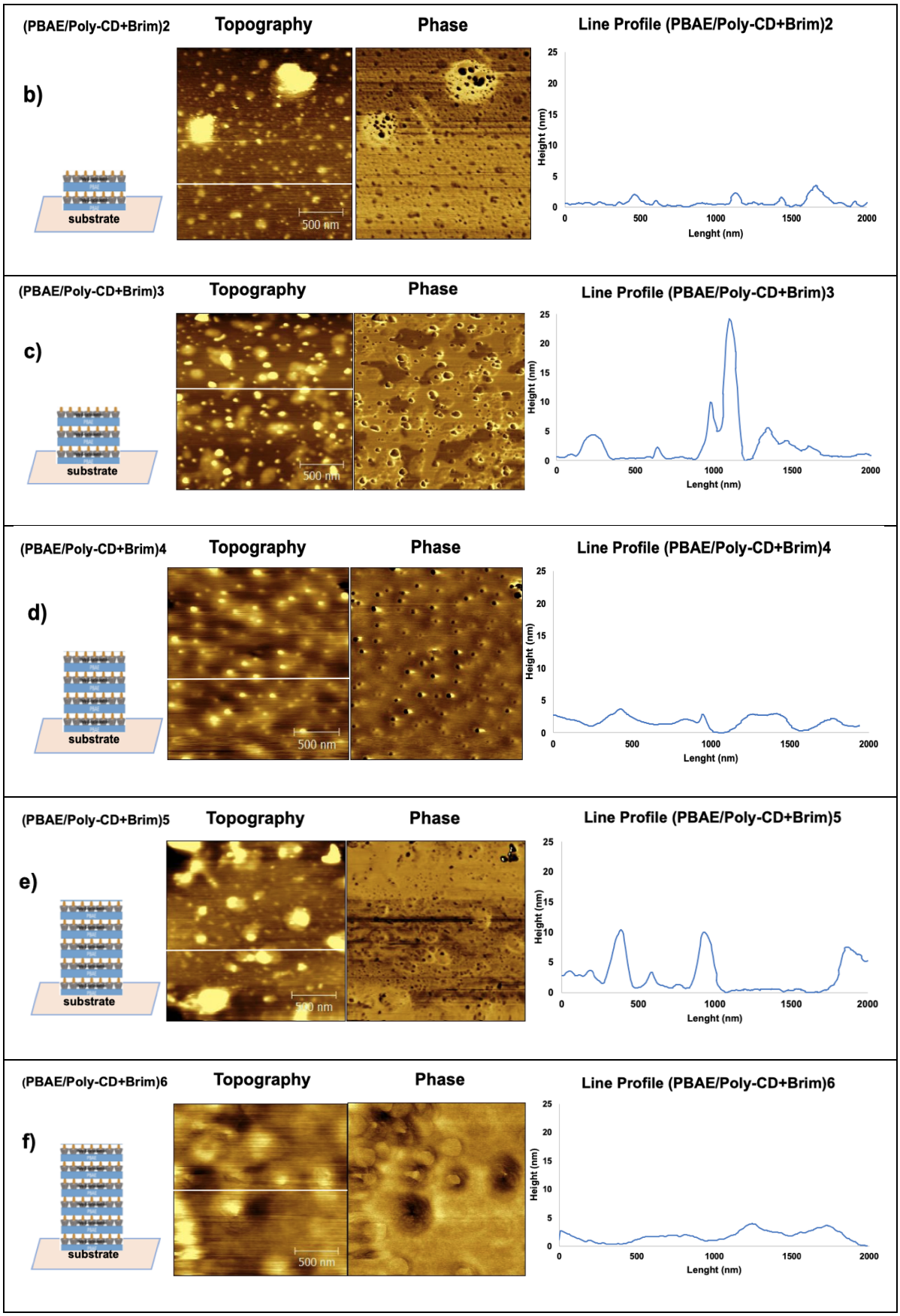
(PBAE/Poly-CD+Brim)2
Topography
Phase
Line Profile (PBAE/Poly-CD+Brim)2
b)
substrate
500 nm
Height (nm)
Lenght (nm)
(PBAE/Poly-CD+Brim)3
Topography
Phase
Line Profile (PBAE/Poly-CD+Brim)3
c)
substrate
500 nm
Height (nm)
Lenght (nm)
(PBAE/Poly-CD+Brim)4
Topography
Phase
Line Profile (PBAE/Poly-CD+Brim)4
d)
substrate
500 nm
Height (nm)
Lenght (nm)
(PBAE/Poly-CD+Brim)5
Topography
Phase
Line Profile (PBAE/Poly-CD+Brim)5
e)
substrate
500 nm
Height (nm)
Lenght (nm)
(PBAE/Poly-CD+Brim)6
Topography
Phase
Line Profile (PBAE/Poly-CD+Brim)6
f)
substrate
500 nm
Height (nm)
Lenght (nm)

In the phase image of the first $(PBAE/Poly\text{-}CD+Brim)_1$ film (Table 2– a)), small grains are observed and the scanned area has a Rrms of 3.031 nm. The first film appears to have a rougher surface than the second $(PBAE/Poly\text{-}CD+Brim)_2$ film (Table 2 – b)), which have a Rrms of 2.239 nm, furthermore, the second $(PBAE/Poly\text{-}CD+Brim)_2$ film also shows small grains the ones observed in the first film, but with a smaller diameter and height. The decrease of roughness suggests a higher affinity of the second bilayer with the previous one creating a smooth coverage of the previous $(PBAE/Poly\text{-}CD+Brim)_1$ bilayer. Regarding the phase image of both films it is possible to identify small dark grains with a different color of the background. This it means that the material located in these darker regions can be different from the background or can be the same material but with a different hardness. At first sight, observing these images, we can admit the hypothesis that the layer is not fully packed and the regions which surround the agglomerates can be associated to the previous bilayer. However, regarding the UV-Vis spectra represented in the Figure 39, we see that the growth of bilayers is uniform and the differences in color observed in the phase images cannot be attributed to the existence of two materials. Therefore, another hypothesis can be formulated and attribute the contrast observed in both images to a different organization of the Poly-CD that may possible can form agglomerates at the surface with a different hardness of the background.

In similar fashion to the $(PBAE/Poly\text{-}CD+Brim)_2$, the $(PBAE/Poly\text{-}CD+Brim)_3$ (Table 2 – c)) also shows a similar surface topography. However, the Rrms of 2.905 nm in this bilayer is higher, indicating a rougher surface relative to the$(PBAE/Poly\text{-}CD+Brim)_2$ with a Rrms of 2.329 nm.

Furthermore, the Rrms result and Line Profile of the $(PBAE/Poly\text{-}CD+Brim)_4$ film (Table 2 – d) Rrms of 1.335 nm indicates a significant decrease in Rrms value, and in turn, a smoother surface, despite maintaining a similar appearance in the topography image to the $(PBAE/Poly\text{-}CD+Brim)_3$ bilayer, as show in Table 1.

Suggesting that the bilayers appear to follow a pattern, where each added bilayer alternates between roughened followed by a smoothed surface, as shown in the profile line of Table 2 and Figure 39. Despite the bilayer surfaces alter between high values and low values of Rrms, the surface grains have a tendency to become progressively smother and lower in height, as the number of bilayers increases: The last $(PBAE/Poly\text{-}CD+Brim)_6$ bilayer surface added (Table 2– f)) was a Rrms of 0.750 nm, being significantly lower compared to the four $(PBAE/Poly\text{-}CD+Brim)_4$ bilayer surface Rrms of 1.335 nm, which in turn, its lower than the second $(PBAE/Poly\text{-}CD+Brim)_2$ bilayer surface Rrms of 2.239 nm. In order to demonstrate this point more clearly, a graph was created with all Rrms values, as show in the Figure 39.

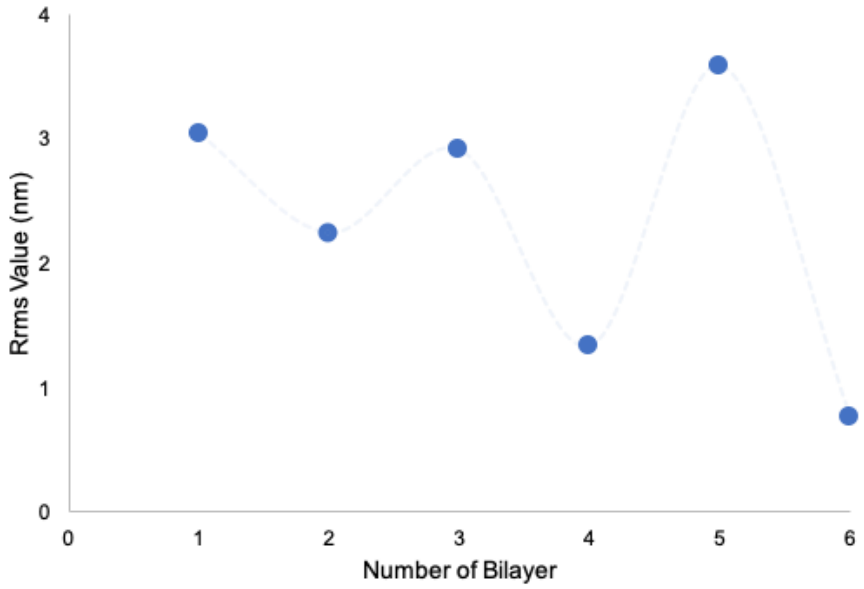

Figure 39 - Rrms Value as a function of the number of bilayers added to the substrate. The line is just to guide the evolution of Rrms values.

In conclusion, the results suggest that as the number of bilayer increases, the ability for the (PBAE(Poly-CD+Brim) to compress and stretch its polymeric chain structure its maintained, allowing for the bilayers to adapt the previous ones, forming a uniform converge over them with no interdiffusion occurring. Wider areas were also scanned and it was observed that the morphology obtained at 2x2 μm^2 was representative of all the film's area (See: AFM images in Appendix - Figure 56, Figure 57,Figure 58,Figure 59,Figure 60 and Figure 61)

3.3 Neutron Reflectivity analysis

The Figure 40 represents the NR curves obtained for 3 different films with one, two and three bilayers. They are very similar and no significant differences can be observed between them. The main reason for this is related with the thickness of each bilayer that can be very smaller and it is hard to differentiate each film. However, the NR of film $(PBAE/Poly\text{-}CD+Brim)_3$ was adjusted with a freeware software StochFit (82) in order to calculate the thickness of each layer.

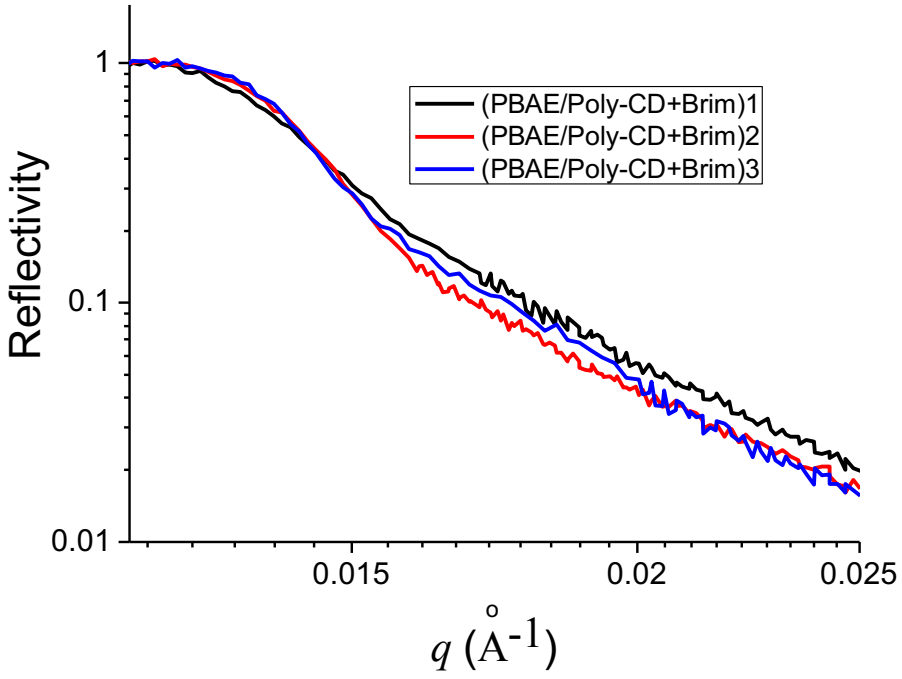

Figure 40 - NR curves of three different films with 1, 2 and 3 bilayers.

The results are resumed in Table 3 and it is possible to observe that the thickness is not constant which means that the conformations of polymers of each layer are different. These can be due to variations in the amount of Brimonidine of each layer that is not always the same. The preparation of the solution of Poly-CD+Brim not takes into account the stoichiometry between the two compounds since we don't know the how many CD are presented in each polymeric chain.

Table 3 - Thickness of each layer presented in a film with 3 bilayers $(PBAE/Poly\text{-}CD+Brim)_3$ determined by fitting the respective MR curve with the StochFit software.

Layer number	Name	Thickness (nm)
1	PBAE	9.8
2	Poly-CD+Brim	9.46
3	PBAE	4.71
4	Poly-CD+Brim	5.03
5	PBAE	8.38
6	Poly-CD+Brim	6.11

Chapter 4 – Brimonidine Kinetic Release

4 Brimonidine Kinetic Release

This chapter describes the Brimonidine kinetic release of four DD films. The release of Brimonidine was analyzed and followed through UV-Vis spectrophotometry using the developed dynamic cell. Two flow rates were tested and compared, Q= 4ml/min and Q=2ml/min. The resulting kinetics graphs that will be demonstrated throughout the chapter.

4.1 Brimonidine release – Q = 4 mL/min

Contrarily to the static mode used in previous works of Brimonidine kinetic release (21, 22), this work applied a dynamic cell in order to mimic the conditions of the ocular environment that possibly could receive the drug.

Three films of $(PBAE/Poly\text{-}CD+Brim)_6$ were prepared and immersed in the dynamic cell to follow the Brimonidine release. The cell was filled with PBS solution with pH= 7,4 and calibrated to a flow rate of Q = 4 mL/min.

The solution was analyzed periodically by UV-Vis spectroscopy, collecting samples with 5 mL each to obtain an absorbance spectrum in order to identify the amount of Brimonidine that was released. Each absorbance spectrum as fitted with a Gaussian function to identify the characteristic band of Brimonidine with accuracy. The Figure 41 shows an absorbance spectrum of Brimonidine in PBS obtained after 900 seconds.

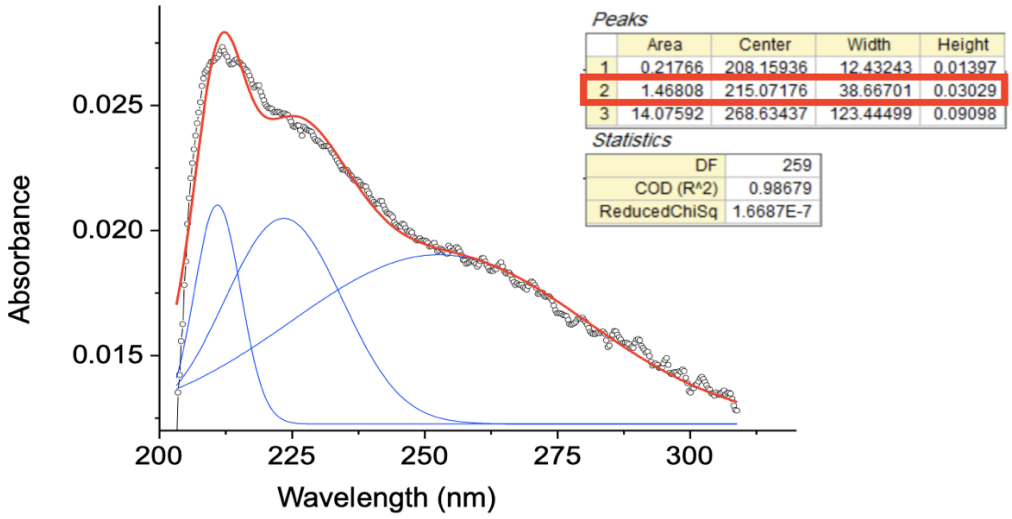

Figure 41 - 900 seconds sample spectra at Q = 4 mL/min with three Gaussian curves fitted and the corresponding peaks values table (upper right corner).

This spectrum was fitted with three Gaussian using the statistical program OriginPro 8® and several interactions were made in order to obtain a low correlation coefficient. The procedure was made for all the observance spectra obtained.

Regarding the obtained absorbance bands, the band at 215 nm was chosen to follow the evolution of Brimonidine during all the kinetic release. The absorption values at 215 nm of all spectra were grouped together in a graphic as a function of time for a maximum of 7200 seconds (2h).

In Figure 42, the amount of Brimonidine released was normalized in order to be comparable with the other experiences, presented in Appendix - Figure 62 and Figure 63.

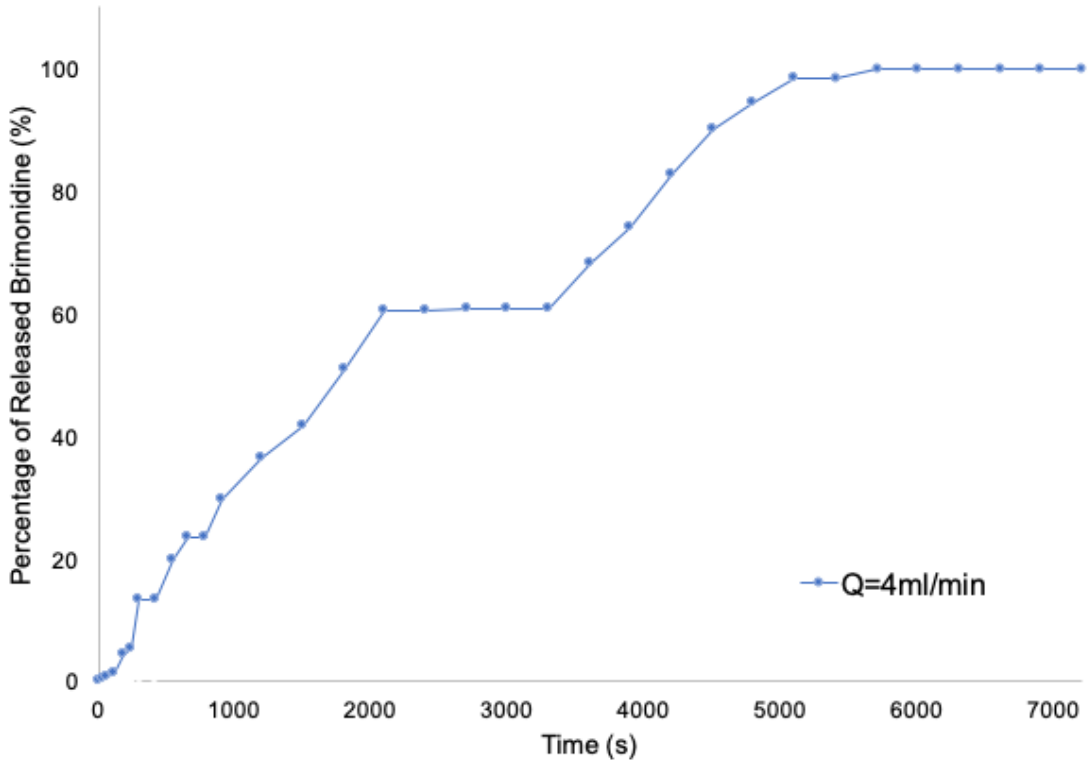

Figure 42 - Normalized values of Brimonidine release kinetics at Q = 4 mL/min for 7200 seconds.

Generally, the profile of the Q = 4mL/min film release demonstrates an increase of Brimonidine overtime in a stratified way, being possible to distinguish six distinct steps during the 7200 seconds kinetic release.

These steps present throughout the kinetics seem to correspond to the moments when there is release of one (PBAE/Poly-CD+Brim) bilayer to the next (PBAE/Poly-CD+Brim) bilayer. In other words, the step moment seems to indicate that the PBAE is responsible for the delay of the (Poly-CD+Brim) layer release, considering that it suffers hydrolysis in aqueous environment.

The Figure 43 summarizes the progressive dissolution of the LbL film under a flow rate of 4 mL/min, where each blue circle corresponds to bilayer desorption and the time (t) that is released.

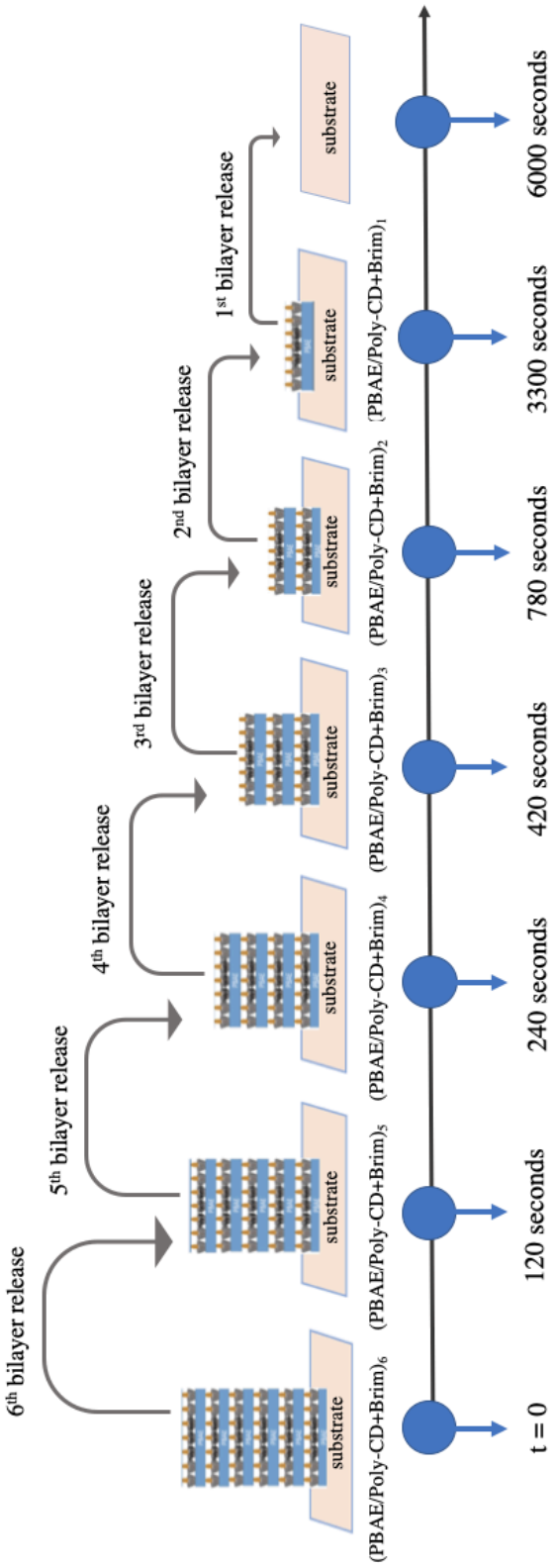

Figure 43 - Schematic representation of (PBAE/Poly-CD+Brim) bilayer release kinetics over time under a Q = 4 mL/min after emersion on to the PBS solution.

4.2 Brimonidine release – Q = 2 mL/min

The influence of a lower flow rate in the Brimonidine release was analyzed and a kinetic release was obtained under a flow rate of Q=2ml/min. The experimental procedure and the data analysis were the same of the experiments with higher flow rate present in the previous sub-chapter. The Figure 44 represents the amount of Brimonidine that was released to the PBS environment and where six distinct steps can be identified.

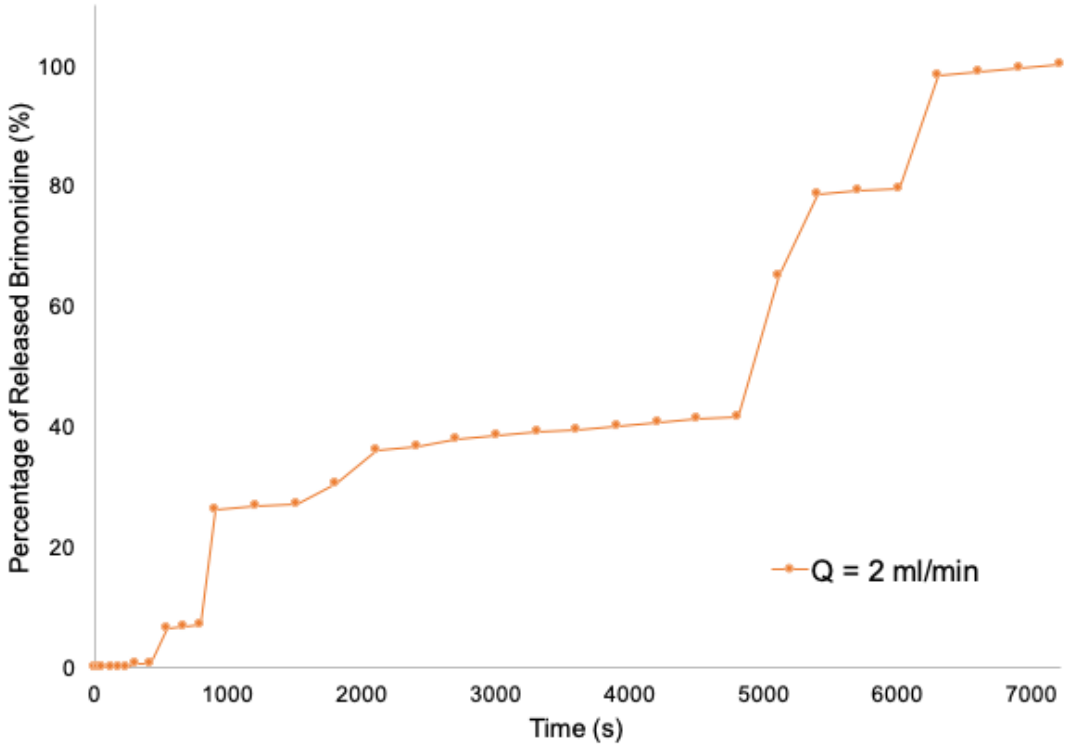

Figure 44 - Normalized values of Brimonidine release kinetics at Q = 2 mL/min for 7200 seconds.

The schema of Figure 43, obtained at higher flow rate summarizes the progressive release of each bilayer, and by comparing with the Figure 45, we note that the release of each bilayer occurs at different times. For this reason, a carefully compression of both kinetics will be displayed on the following sub-chapter.

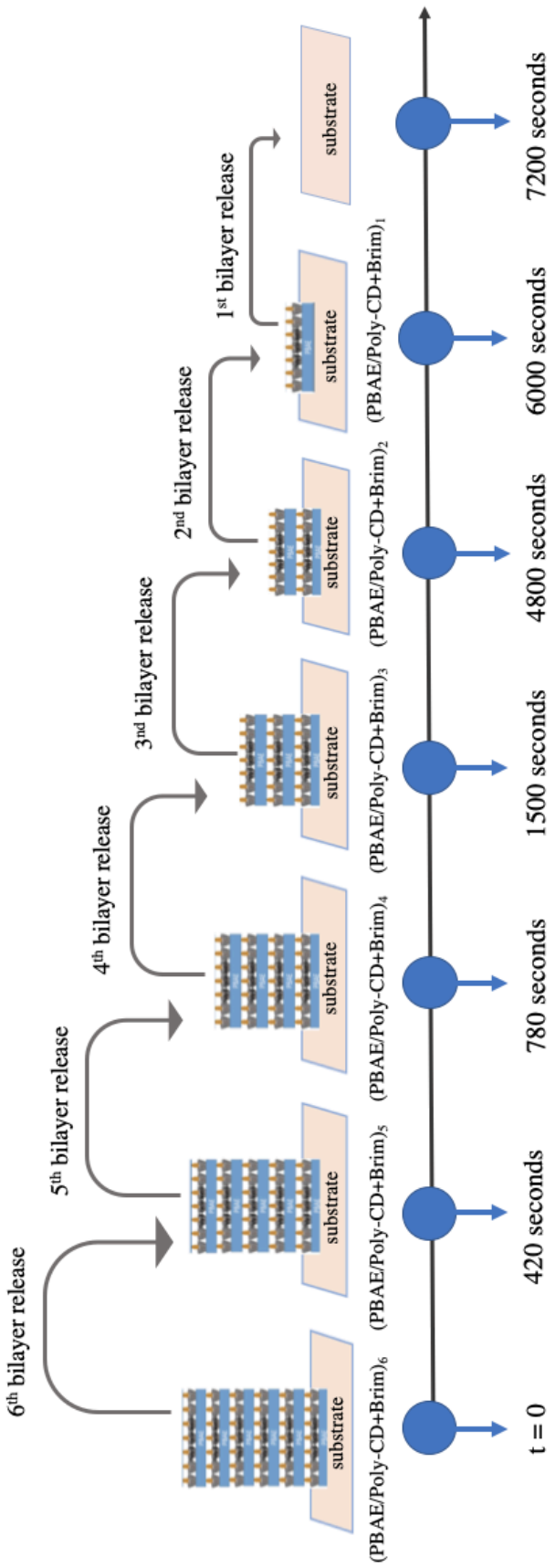

Figure 45 - Schematic representation of (PBAE/Poly-CD+Brim) bilayer release kinetics over time under Q = 2 mL/min after emersion on to the PBS solution.

4.3 Analysis of flow rate effect

By analyzing the Figure 46, which compares the amount of Brimonidine delivered at Q = 4 mL / min and at Q = 2 mL / min, it is possible to observe that in both conditions the Brimonidine release is a stepwise procedure, where each bilayer is released at a specific period of time.

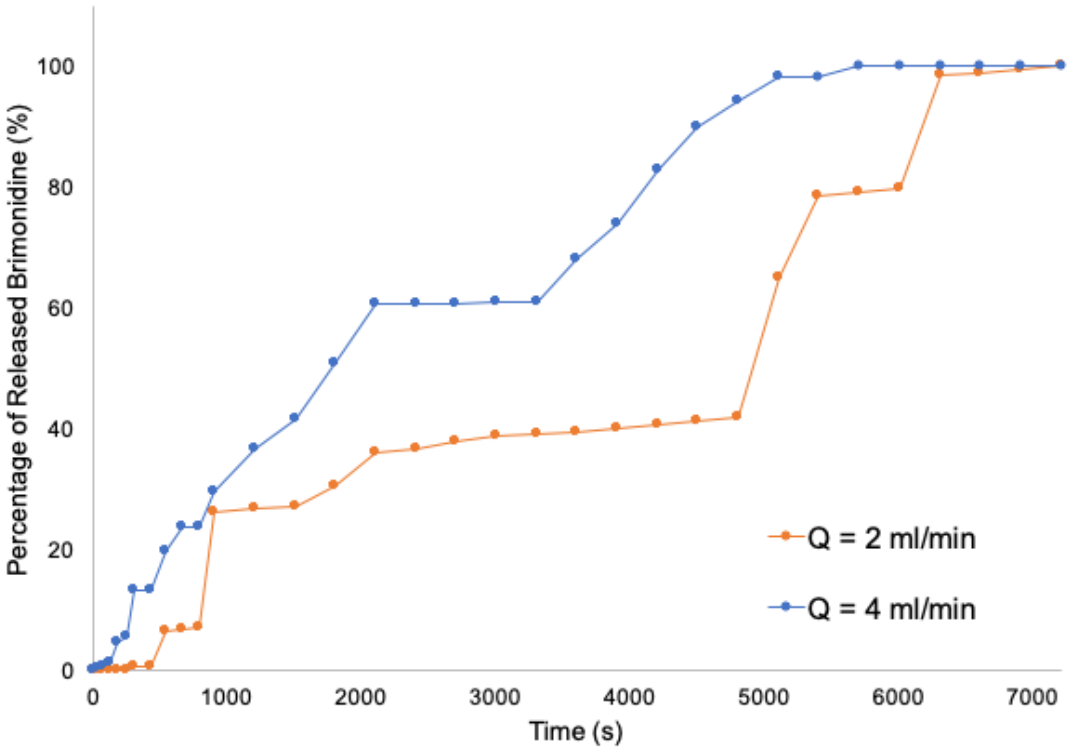

Figure 46 - Normalized amount of Brimonidine release at flow rates of Q = 4 mL/min and Q = 2 mL/min.

The PBAE has an important role in this process since it is the responsible to avoid a disorganized drug release, ensuring that a precise amount is delivered at a specific period of time. In more detail, by observing the Table 4, which comprises the steps of both kinetics, we observe significant differences from the graph Table 4 - a), which represents the kinetics for the first 500s. It is possible to observe that at in the higher flow rate the release is more faster in comparison with the experiment at lower flow rate. For the experiment, the Q = 4 mL/min initial step occurs during the first 100 seconds while at Q = 2 mL / min the first step occurs only after 250 seconds.

Table 4 - Representation of step-by-step of Brimonidine release kinetics with the identification of a release of each bilayer.

a) Release of 6th bilayer	b) Release of 5th bilayer
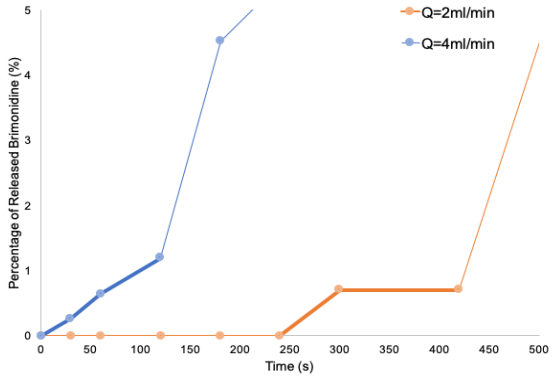	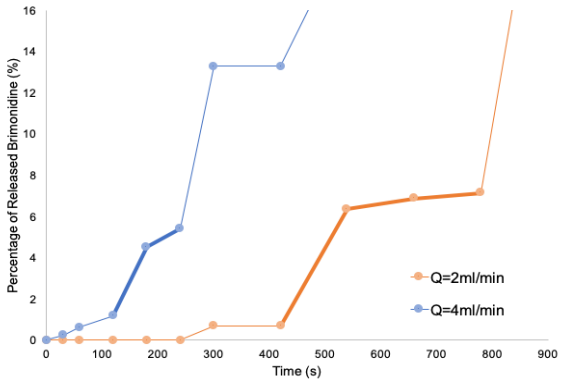
c) Release of 4th bilayer	**d) Release of 3rd bilayer**
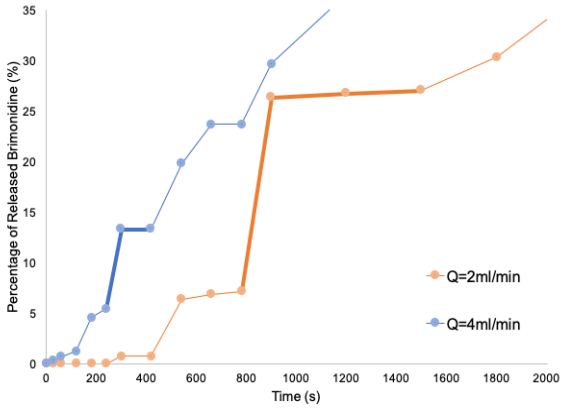	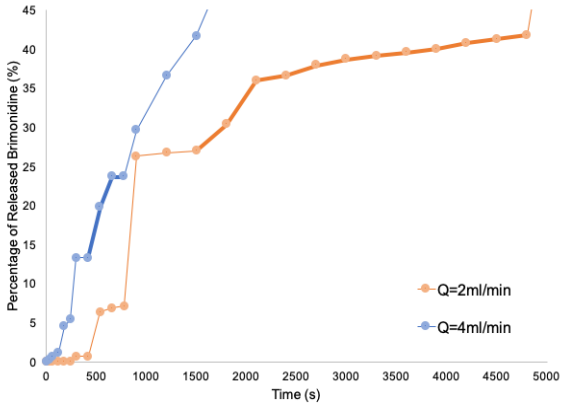
e) Release of 2nd bilayer	**f) Release of 1st bilayer**
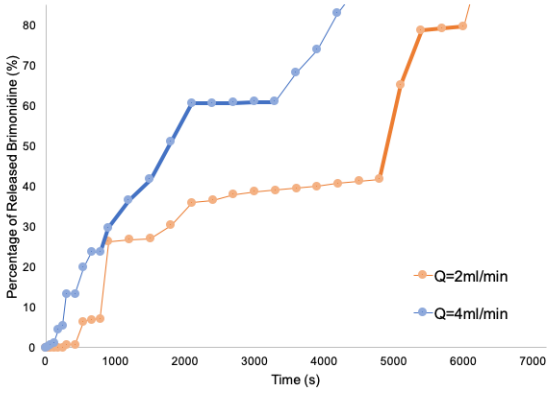	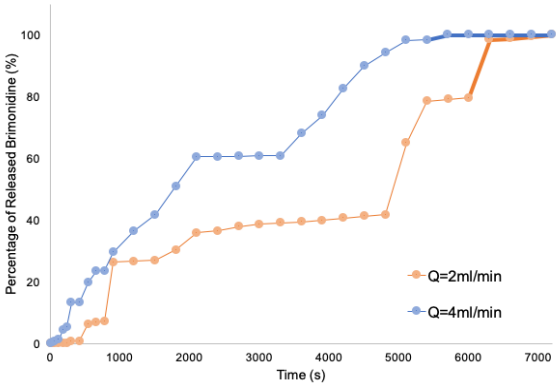

For the 5th bilayer (Table 4 – b), the second step appears earlier in Q = 4 mL/min, between 120 seconds and 240 seconds, and for the Q = 2 mL/min appears between 420 seconds and 780 seconds.

However, as it can be observed in the graph, the step duration of Q = 2 mL/min in comparison to the higher flow rate is significantly longer, taking 360 seconds to form the full step in comparison to the 120 seconds it took Q = 4 mL/min. This observation is later corroborated when observing the remaining steps: Where Q = 2 mL/min has steps with durations in time greater than Q = 4 mL/min in almost all the steps analyze. Giving the possible indication that the flow rate not only affects the Brimonidine release time, but also its release duration.

For the following bilayer, the same behavior occurs, *i.e,* the Brimonidine release occurs earlier and faster in the higher flow rate when compared with the same situation at the lower flow rate.

The Figure 47 resumes the evolution of the amount of drug that is released at a certain time. In the bar graph, is possible to identify the main difference between both kinetics it's that at a lower flow rate occurs a delay in the release of each bilayer. In both cases we observed that the Δt it not constant and this can be related with the morphology characteristics in the surface of each bilayer.

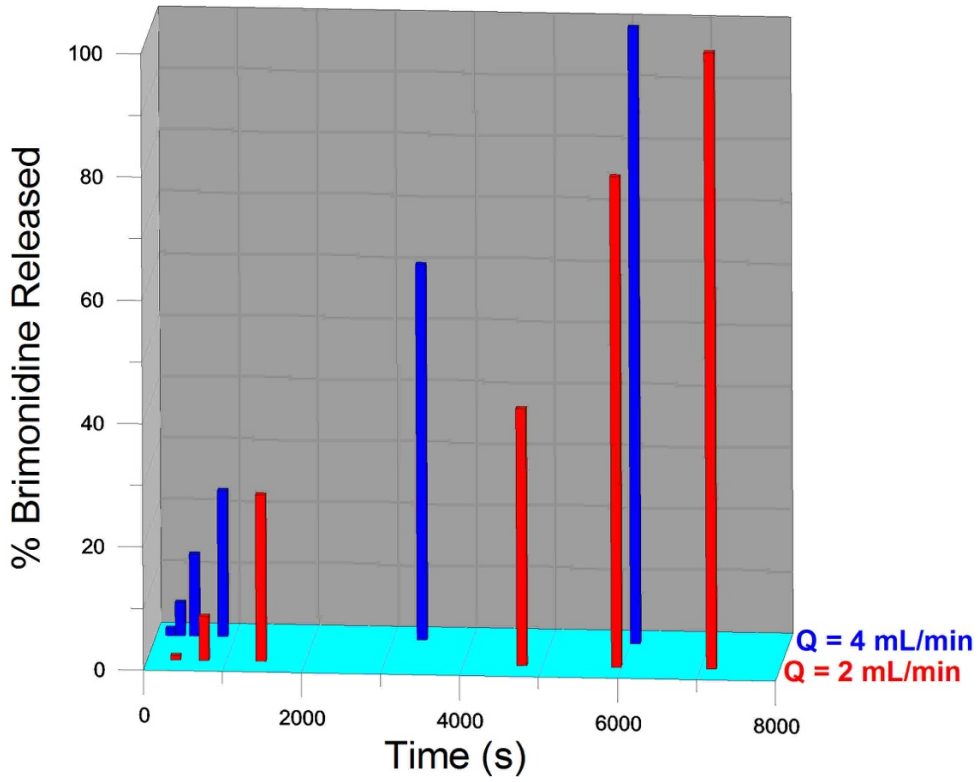

Figure 47 - Percentage of released Brimonidine in relation to time for each step in Q = 4 mL/min and Q = 2 mL/min.

Regarding the evolution of Rrms presented in Figure 39, which indicates a decrease of roughness as a function of the number of bilayer, it is possible to correlate this result with the increase in the Δt observed after 780 seconds. The decrease of Rrms suggest a higher organization of polymeric chains considering that they can be more stretched and consequently originate an easier release. However, the Δt between each bilayer is not constant due to the heterogeneity of each bilayer thickness, as can be observed in the results by NR present in Table 3.

Chapter 5 – Conclusions

5 Conclusions

In this thesis, a dynamic cell to study a drug release in real time was designed and fabricated. This work involved the preparation of DD films composed of layers of Brimonidine encapsulated in Poly-CD alternated with barrier layers of PBAE prepared by the LbL technique. They were characterized by UV-Vis spectroscopy, AFM and NR. More specifically, the growth of each bilayer was demonstrated by analyzing its absorption spectra and the results demonstrated a uniform and reproducible growth. The AFM analysis of each bilayer revealed a decrease of Rrms as a function of the number of bilayers, suggesting an increase in the polymeric chains organization. However, the NR results regarding the thickness of each layer showed that the thickness is not constant that can be related with the difficulty to maintain the same amount of Brimonidine at each bilayer since the preparation of the solution with Poly-CD and Brimonidine not taking into account the same stoichiometry between the two molecules.

These films were tested using the fabricated dynamic cell. Its design and fabrication involved several stages until achieving the final prototype cell. A final dynamic cell was obtained that allowed the monitorization of the Brimonidine release in real-time, and it was demonstrated that with this system is possible to follow the release of each bilayer that is resented in the film.

The fabricated dynamic cell is a clear innovation of the state of art considering that previous works that used a static system were not demonstrated a drug stepwise release with the identification of the release of each bilayer.

Two flow rates were tested, one at Q = 4mL/min and another one at Q = 2mL/min, both kinetics demonstrated an increase of Brimonidine overtime in a stratified way and six distinct steps were identified. Significant differences between the two kinetics were observed considering that the kinetic at lower flow rate presents a slower release.

The developed dynamic cell demonstrated that is a versatile system that can be applied for any drug delivery system and it can allow a correct drug release monitorization. In this case, the developed configuration is more representative of the correct flow rate present in the ocular region that and that will receive the Brimonidine multilayer film.

Chapter 6 – Future Work

6 Future Work

The use of a dynamic cell printed on a 3D printer proved to be a viable platform for the kinetics study of DD films. Ideally, the cell should be installed inside of spectrophotometer for a direct absorbance reading, eliminating the need to take samples. This improvement can be the following step.

In conclusion, this work took the first steps in the dynamic release of DD films using custom 3D printing cells and helped to understand how design and flow affect kinetics film release in to the medium. Nevertheless, more experiments are required to understand in greater detail the mechanisms involved in the drug release.

Bibliography

1. Anderski J, Mahlert L, Sun J, Birnbaum W, Mulac D, Schreiber S, et al. Light-responsive nanoparticles based on new polycarbonate polymers as innovative drug delivery systems for photosensitizers in PDT. Int J Pharm. 2019;557:182-91.
2. Lee J, Kong M, Kim J, Kee C. Comparison of visual field progression between relatively low and high intraocular pressure groups in normal tension glaucoma patients. J Glaucoma. 2014;23(8):553-60.
3. Wang Y, Lu W, Yan T, Zhou J, Xie Y, Yuan J, et al. Functional MRI reveals effects of high intraocular pressure on central nervous system in high-tension glaucoma patients. Acta Ophthalmol. 2019.
4. Sah AK, Suresh PK. Medical management of glaucoma: focus on ophthalmologic drug delivery systems of timolol maleate. Artif Cell Nanomed B. 2017;45(3):448-59.
5. Quigley HA, Broman AT. The number of people with glaucoma worldwide in 2010 and 2020. Brit J Ophthalmol. 2006;90(3):262-7.
6. Pita-Thomas DW, Goldberg JL. Nanotechnology and glaucoma: little particles for a big disease. Curr Opin Ophthalmol. 2013;24(2):130-5.
7. Casson RJ, Chidlow G, Wood JP, Crowston JG, Goldberg I. Definition of glaucoma: clinical and experimental concepts. Clin Exp Ophthalmol. 2012;40(4):341-9.
8. De TK, Rodman DJ, Holm BA, Prasad PN, Bergey EJ. Brimonidine formulation in polyacrylic acid nanoparticles for ophthalmic delivery. Journal of Microencapsulation. 2003;20(3):361-74.
9. Adkins JC, Balfour JA. Brimonidine. A review of its pharmacological properties and clinical potential in the management of open-angle glaucoma and ocular hypertension. Drugs Aging. 1998;12(3):225-41.
10. Gooch N, Molokhia SA, Condie R, Burr RM, Archer B, Ambati BK, et al. Ocular drug delivery for glaucoma management. Pharmaceutics. 2012;4(1):197-211.
11. Gilhotra SGRM. Enhancement of anti-glaucoma potential by novel ocular drug delivery system. International Journal of Pharmacy and Pharmaceutical Sciences. 2011;3(2):55-8.
12. S. Naveed SF, S. S. Abbas, S. H. Jawed, F. Qamar, M. Y. Hussain, and I. Ali. Contemporary trends in novel ophthalmic drug delivery system: An overview. OALib.

2015;2(05):1-10.

13. Guzman-Aranguez A, Colligris B, Pintor J. Contact lenses: promising devices for ocular drug delivery. J Ocul Pharmacol Ther. 2013;29(2):189-99.
14. K. Rajurkar SD, P. P. Gupta, D. John, and L. Chauhan. Compliance to topical anti-glaucoma medications among patients at a tertiary hospital in North India. J Curr Ophthalmol. 2018;30(2):125-9.
15. Cardigos J, Ferreira Q, Crisostomo S, Moura-Coelho N, Cunha JP, Pinto LA, et al. Nanotechnology-Ocular Devices for Glaucoma Treatment: A Literature Review. Curr Eye Res. 2019;44(2):111-7.
16. Sahoo SK, Dilnawaz F, Krishnakumar S. Nanotechnology in ocular drug delivery. Drug Discov Today. 2008;13(3-4):144-51.
17. Xinming L, Yingde C, Lloyd AW, Mikhalovsky SV, Sandeman SR, Howel CA, et al. Polymeric hydrogels for novel contact lens-based ophthalmic drug delivery systems: a review. Cont Lens Anterior Eye. 2008;31(2):57-64.
18. Gulsen D, Li CC, Chauhan A. Dispersion of DMPC liposomes in contact lenses for ophthalmic drug delivery. Curr Eye Res. 2005;30(12):1071-80.
19. Sun J, Lei Y, Dai Z, Liu X, Huang T, Wu J, et al. Sustained Release of Brimonidine from a New Composite Drug Delivery System for Treatment of Glaucoma. ACS Appl Mater Interfaces. 2017;9(9):7990-9.
20. Franca JR, Foureaux G, Fuscaldi LL, Ribeiro TG, Rodrigues LB, Bravo R, et al. Bimatoprost-loaded ocular inserts as sustained release drug delivery systems for glaucoma treatment: in vitro and in vivo evaluation. Plos One. 2014;9(4):e95461.
21. Araújo MnSdC. Nanostructured films for controlled release of drugs for glaucoma treatment: Instituto Superior Técnico; 2016.
22. Morais HIC. Nanostructured films of graphene for controlled ocular drug delivery: Instituto Superior de Engenharia de Lisboa; 2017.
23. Monica Machado GAS, Diogo B. Bitoque, Joana Ferreira, Luís A. Pinto,, Ferreira JMaQ. Self-Assembled Multilayer Films for Time-Controlled Ocular Drug Delivery. ACS Appl Bio Mater. 2019;2:4173−80.
24. Allen TM, Cullis PR. Drug delivery systems: entering the mainstream. Science. 2004;303(5665):1818-22.
25. Unagolla JM, Jayasuriya AC. Drug transport mechanisms and in vitro release kinetics of vancomycin encapsulated chitosan-alginate polyelectrolyte microparticles as a

controlled drug delivery system. Eur J Pharm Sci. 2018;114:199-209.

26. Jain KK. Drug delivery systems - an overview. Methods Mol Biol. 2008;437:1-50.
27. N. Rajgor VB, and M. Patel. Implantable drug delivery systems: An overview. Systematic Reviews in Pharmacy. 2011;2:91.
28. Raposo M, Oliveira ON. Energies of adsorption of poly(o-methoxyaniline) layer-by-layer films. Langmuir. 2000;16(6):2839-44.
29. Ferreira Q, Ribeiro PA, Oliveira ON, Raposo M. Long-Term Stability at High Temperatures for Birefringence in PAZO/PAH Layer-by-Layer Films. Acs Appl Mater Inter. 2012;4(3):1470-7.
30. S. Oliveira ONJH, J.-A.; Zucolotto, V.; Balasubramanian, S.; Li, L.; Nalwa, H.S.; Kumar, J.; Tripathy. Layer-by-layer polyelectrolyte-based thin films for electronic and photonic applications.2002.
31. K. Hala´sz YH, and L. Cso´ka. Reducing water vapor permeability of poly(lactic acid) film and bottle through layer-by-layer deposition of green-processed cellulose nanocrystals and chitosan. International Journal of Polymer Science. 2015;2015:1-6.
32. Iler RK. Multilayers of colloidal particles. J Colloid Interf Sci. 1966;21(6):569-94.
33. Thomas IM. Single-layer TiO2 and multilayer TiO2–SiO2 optical coatings prepared from colloidal suspensions. Applied Optics. 1987;26(21):4688-91
34. Schlenoff JB, Dubas ST, Farhat T. Sprayed polyelectrolyte multilayers. Langmuir. 2000;16(26):9968-9.
35. Sun JQ, Gao MY, Feldmann J. Electric field directed layer-by-layer assembly of highly fluorescent CdTe nanoparticles. J Nanosci Nanotechno. 2001;1(2):133-6.
36. Lee D, Rubner MF, Cohen RE. All-nanoparticle thin-film coatings. Nano Lett. 2006;6(10):2305-12.
37. Decher G. Fuzzy nanoassemblies: Toward layered polymeric multicomposites. Science. 1997;277(5330):1232-7.
38. D. Dey MNI, S.A. Hussain and D. Bhattacharjee. Layer by Layer (LbL) Technique for fabrication of electrostatic Self assembled ultrathin films International Journal of Pure and Applied Physics 2008;4(1):39-44.
39. Wimmer T. Cyclodextrins. Ullmann's Encyclopedia of Industrial Chemistry: Wiley-VCH; 2012.
40. Oliveri V, Vecchio G. Cyclodextrins as Protective Agents of Protein Aggregation: An

Overview. Chem-Asian J. 2016;11(11):1648-57.

41. Challa R, Ahuja A, Ali J, Khar RK. Cyclodextrins in drug delivery: An updated review. Aaps Pharmscitech. 2005;6(2).

42. Davis ME, Brewster ME. Cyclodextrin-based pharmaceutics: past, present and future. Nat Rev Drug Discov. 2004;3(12):1023-35.

43. Sigma-Aldrich. β-Cyclodextrin polymer 2019 [Available from: https://www.sigmaaldrich.com/catalog/product/sigma/c2485?lang=pt&region=PT.

44. Langer DMLaR. Degradable poly (beta-amino esters): Synthesis , characterization , and self-assembly with plasmid dna. J Am Chem Soc. 2000;122(10):10 781 - 10 68.

45. Liu Y, Li Y, Keskin D, Shi L. Poly(beta-Amino Esters): Synthesis, Formulations, and Their Biomedical Applications. Adv Healthc Mater. 2019;8(2):e1801359.

46. Burke J, Schwartz M. Preclinical evaluation of brimonidine. Surv Ophthalmol. 1996;41:S9-S18.

47. Aburahma MH, Mahmoud AA. Biodegradable ocular inserts for sustained delivery of brimonidine tartarate: preparation and in vitro/in vivo evaluation. AAPS PharmSciTech. 2011;12(4):1335-47.

48. Cantor LB, Burke J. Brimonidine. Expert Opin Investig Drugs. 1997;6(8):1063-83.

49. Miladi K, Ibraheem D, Iqbal M, Sfar S, Fessi H, Elaissari A. Particles from Preformed Polymers as Carriers for Drug Delivery. Excli J. 2014;13:28-57.

50. Loftsson T, Brewster ME. Pharmaceutical applications of cyclodextrins .1. Drug solubilization and stabilization. Journal of Pharmaceutical Sciences. 1996;85(10):1017-25.

51. Esther Y.Chen WFL, loreto Megido, Paula Díez, Manuel Fuentes, Cecilia Fager, Eva Olsson, Isabel Gessner, Sanjay Mathur. Chapter 3 - Understanding and utilizing the biomolecule/nanosystems interface. Nanotechnologies in Preventive and Regenerative Medicine. 2018(2018):207-97.

52. Mosorov V. The Lambert-Beer law in time domain form and its application. Appl Radiat Isot. 2017;128:1-5.

53. Perkampus H-H. UV-VIS Spectroscopy and Its Applications. 1ª ed2013.

54. Mavrodineanu RWBaR. Acidic Potassium Dichromate Solutions as Ultraviolet Absorbance Standards. Journal Of Research Of The National Bureau Of Standards. 1976;No.4.

55. Dufrene YF, Ando T, Garcia R, Alsteens D, Martinez-Martin D, Engel A, et al. Imaging modes of atomic force microscopy for application in molecular and cell biology. Nat Nanotechnol. 2017;12(4):295-307.

56. Jalili NL, K A review of atomic force microscopy imaging systems: application to molecular metrology and biological sciences. Mechatronics. 2004;14(8):907-45.

57. Brandl F, Sommer F, Goepferich A. Rational design of hydrogels for tissue engineering: impact of physical factors on cell behavior. Biomaterials. 2007;28(2):134-46.

58. Ben Ammar H. Investigation of ternary AlInN and quaternary AlGaInN alloys for High Electron Mobility Transistors by Transmission Electron Microscopy 2017 [

59. Scott W. Use of phase imaging in atomic force microscopy for measurement of viscoelastic contrast in polymer nanocomposites and molecularly thick lubricant films. Ultramicroscopy. 2003;97:151-69.

60. Narchi P. nvestigation of crystalline silicon solar cells at the nano-scale using scanning probe microscopy techniques 2016 [

61. JH CLNCL. Examining protein–lipid complexes using neutron scattering. Methods Mol Biol,. 2013:119 - 50.

62. Chennevière FCA. Neutron reflectivity for soft matter. EPJ Web of Conferences 188; France 2018.

63. Torikai N, Yamada NL, Noro A, Harada M, Kawaguchi D, Takano A, et al. Neutron reflectometry on interfacial structures of the thin films of polymer and lipid. Polym J. 2007;39(12):1238-46.

64. T.P.Russell. X-ray and neutron reflectivity for the investigation of polymers. Materials Science Reports. 1990;5(4):171-271.

65. Neutron Reflectivity 2019 [updated 11/25/2019. Available from: https://www.nffa.eu/offer/characterisation/installation-4/neutron-reflectivity/.

66. D. W. Lee T-KH, D. Kang, J. Lee, M. Heo, J. Y. Kim, B.-S. Kim, and H. S. Shin. Highly controllable transparent and conducting thin films using layer-by-layer assembly of oppositely charged reduced graphene oxides. Mater Chem. 2011;21(10):3438 - 42.

67. Schubert C, van Langeveld MC, Donoso LA. Innovations in 3D printing: a 3D overview from optics to organs. Brit J Ophthalmol. 2014;98(2):159-61.

68. Jain MTPK. Role of build orientation in layered manufacturing: a review. International Journal of Manufacturing Technology and Management. 2013;27(1/2/3):47-73.

69. Bikas H, Stavropoulos P, Chryssolouris G. Additive manufacturing methods and modelling approaches: a critical review. Int J Adv Manuf Tech. 2016;83(1-4):389-405.

70. Carneiro OS, Silva AF, Gomes R. Fused deposition modeling with polypropylene. Mater Design. 2015;83:768-76.

71. Patel HHHSASAABA. 3D printable conductive materials for the fabrication of electrochemical sensors: A mini review. Electrochemistry Communications. 2016;96:27-31.

72. Jones R, Haufe P, Sells E, Iravani P, Olliver V, Palmer C, et al. RepRap - the replicating rapid prototyper. Robotica. 2011;29:177-91.

73. Autodesk Tinkercad 2019 [Available from: https://www.tinkercad.com/.

74. Goldsmith JA, Li Y, Chalita MR, Westphal V, Patil CA, Rollins AM, et al. Anterior chamber width measurement by high speed optical coherence tomography. Ophthalmology. 2005;112(2):238-44.

75. Roy A, Kar M, Mandal D, Ray RS, Kar C. Variation of Axial Ocular Dimensions with Age, Sex, Height, BMI-and Their Relation to Refractive Status. Journal of Clinical and Diagnostic Research. 2015;9(1):Ac1-Ac4.

76. Ruben M. Contact-Lens in Practice. Ann Ophthalmol. 1981;13(3):289-95.

77. Montes-Mico R. Role of the tear film in the optical quality of the human eye. J Cataract Refract Surg. 2007;33(9):1631-5.

78. Mishima S, Gasset A, Klyce SD, Jr., Baum JL. Determination of tear volume and tear flow. Invest Ophthalmol. 1966;5(3):264-76.

79. McCulley JP, Shine WE. The lipid layer: the outer surface of the ocular surface tear film. Biosci Rep. 2001;21(4):407-18.

80. Reynolds O. An experimental investigation of the circumstances which determine whether the motion of water shall be direct or sinuous, and of the law of resistance in parallel channels. 174: The Royal Society; 1883. p. 935-82.

81. German EJ, Hurst MA, Wood D. Reliability of drop size from multi-dose eye drop bottles: is it cause for concern? Eye (Lond). 1999;13 (Pt 1):93-100.

82. S.M. Danauskas DL, M. Meron, B. Lin and K.Y.C. Lee. Stochastic fitting of specular x-ray reflectivity data using StochFit. . Appl Cryst. 2008;41:1187-93.

Appendix

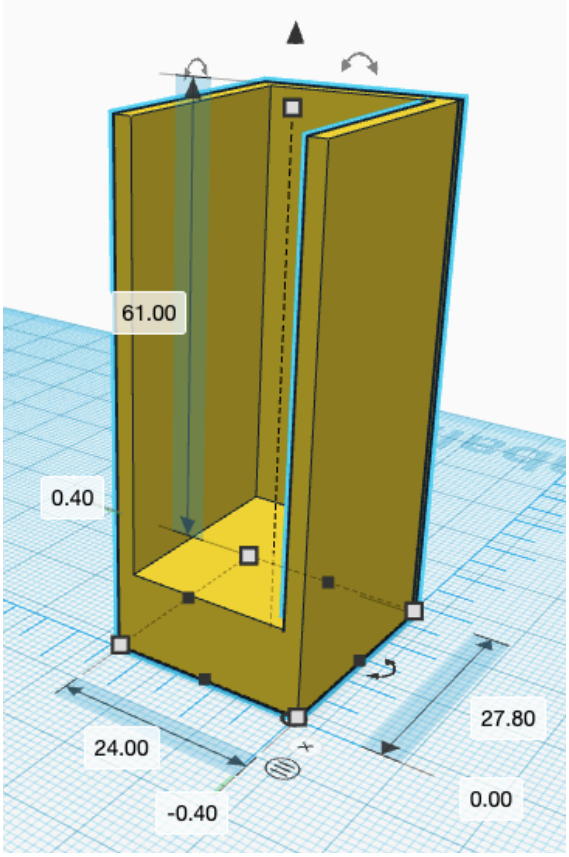

Figure 48 - Schematic representation of the inner part of the 1ª prototype cell in a different angle.

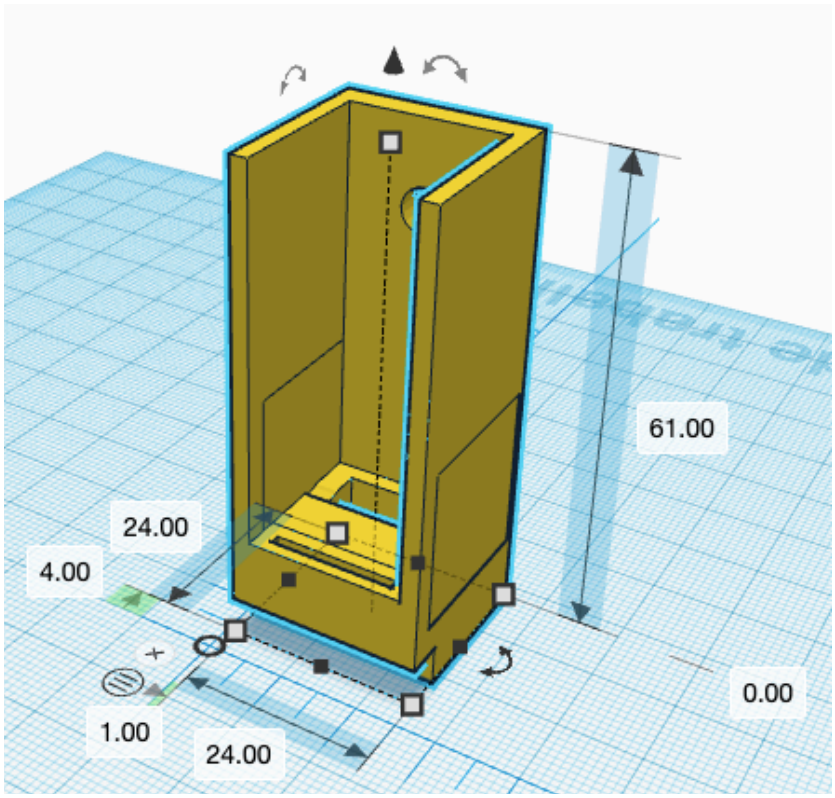

Figure 49 - Schematic representation of the inner part of the 2ª prototype cell in a different angle.

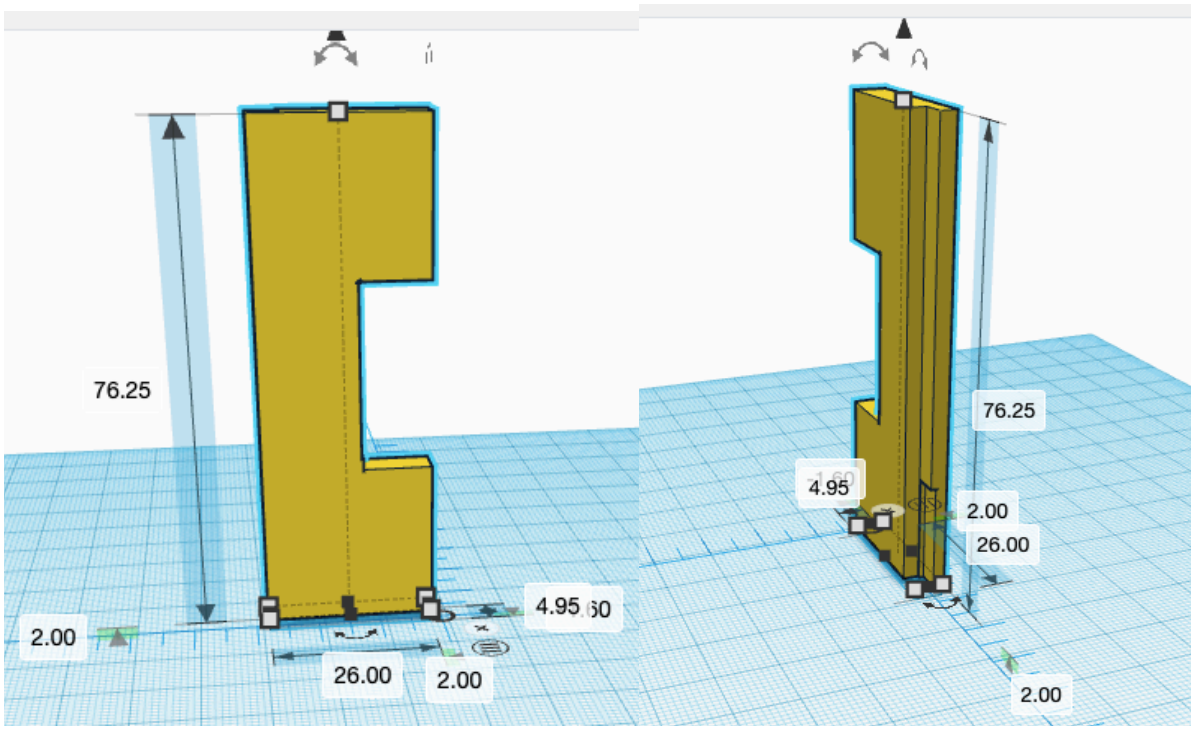

Figure 50 - Schematic representation of docking bracket prototype in different angles.

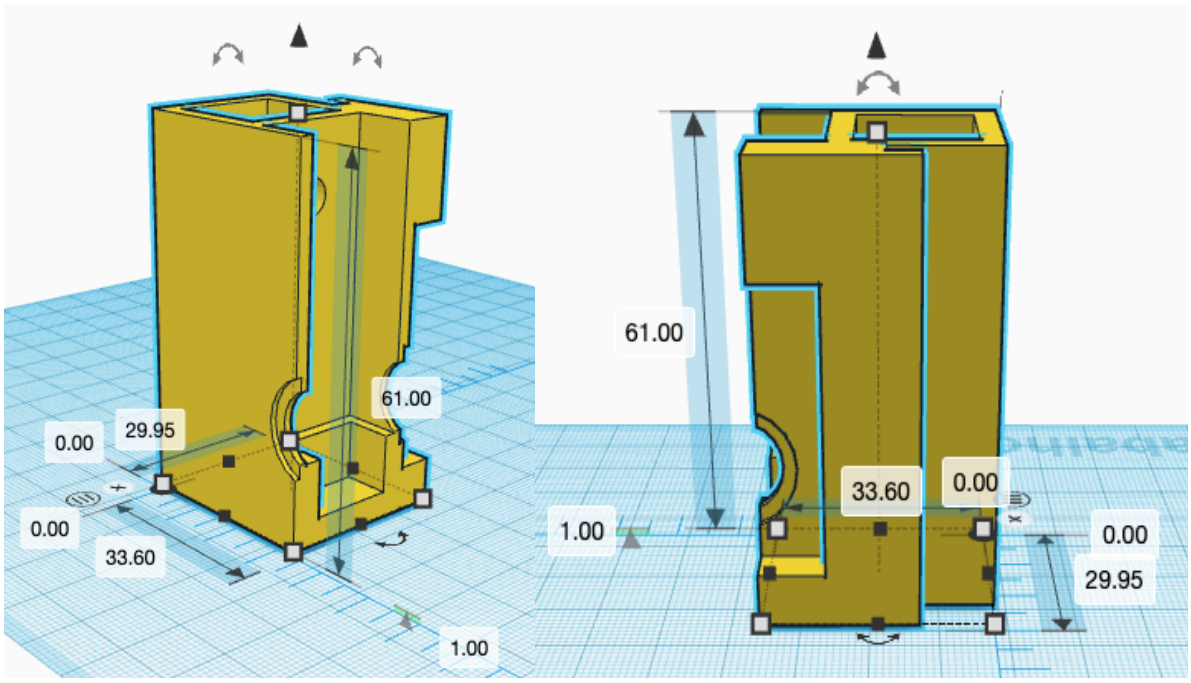

Figure 51 - Schematic representation of the inner and outer parts of the 3ª prototype cell in different angles.

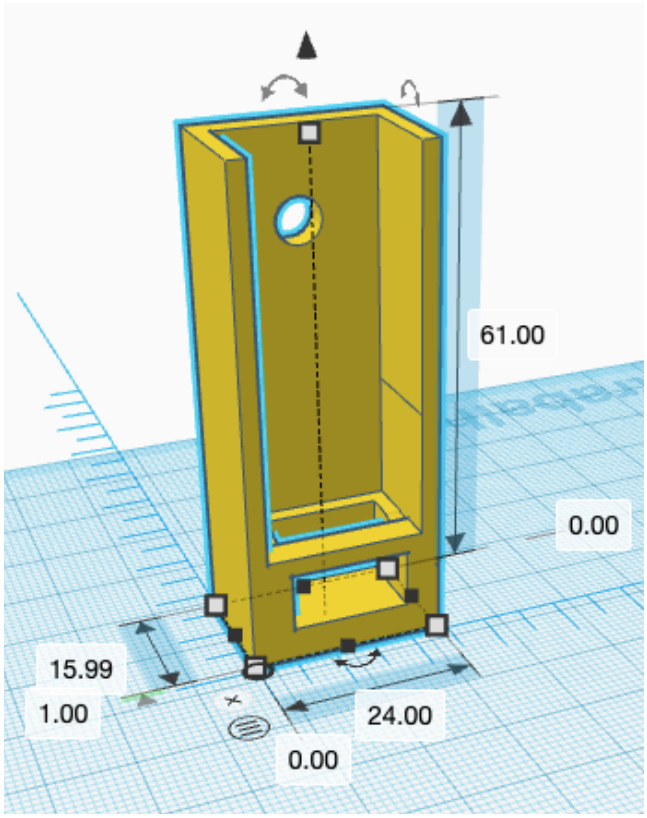

Figure 52 - Schematic representation of the inner part of the final prototype cell in a different angle.

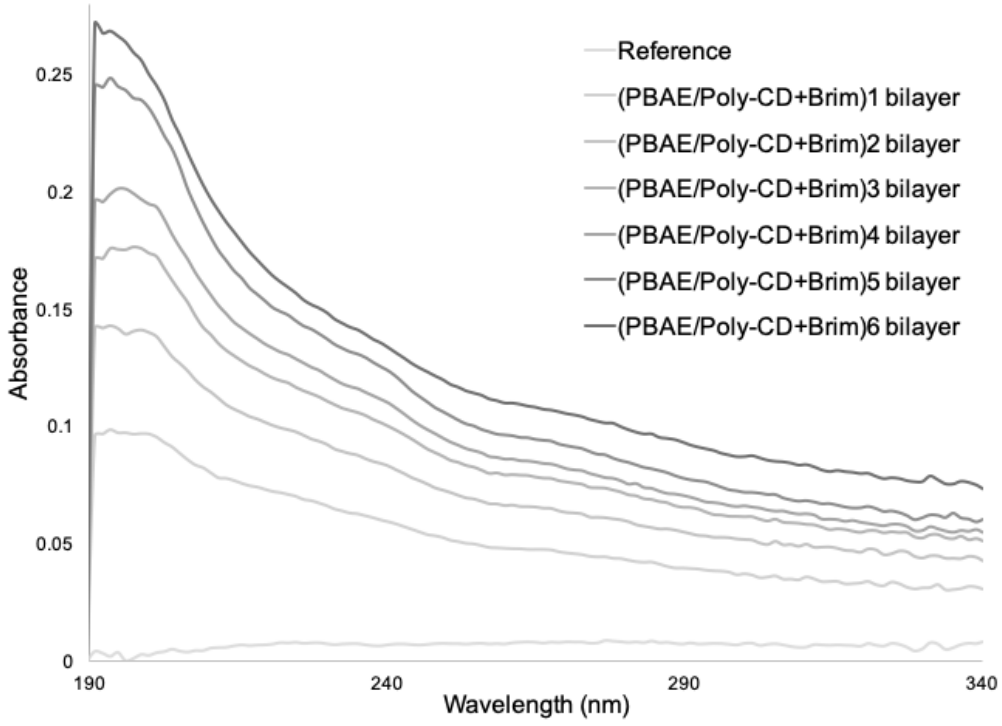

Figure 53 - Absorption spectra of six (PBAE/Poly-CD+Brim) bilayer of the 4st LbL Film, obtained after each bilayer deposition.

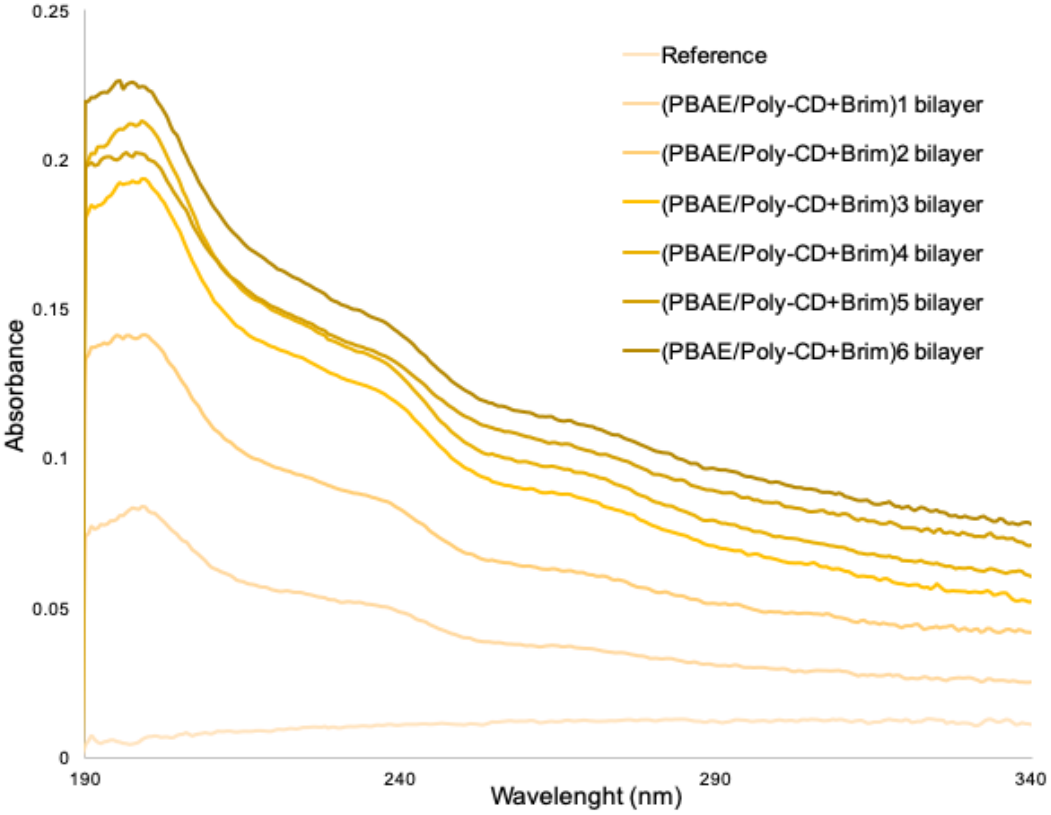

Figure 54 - Absorption spectra of six (PBAE/Poly-CD+Brim) bilayer of the 3st LbL Film, obtained after each bilayer deposition.

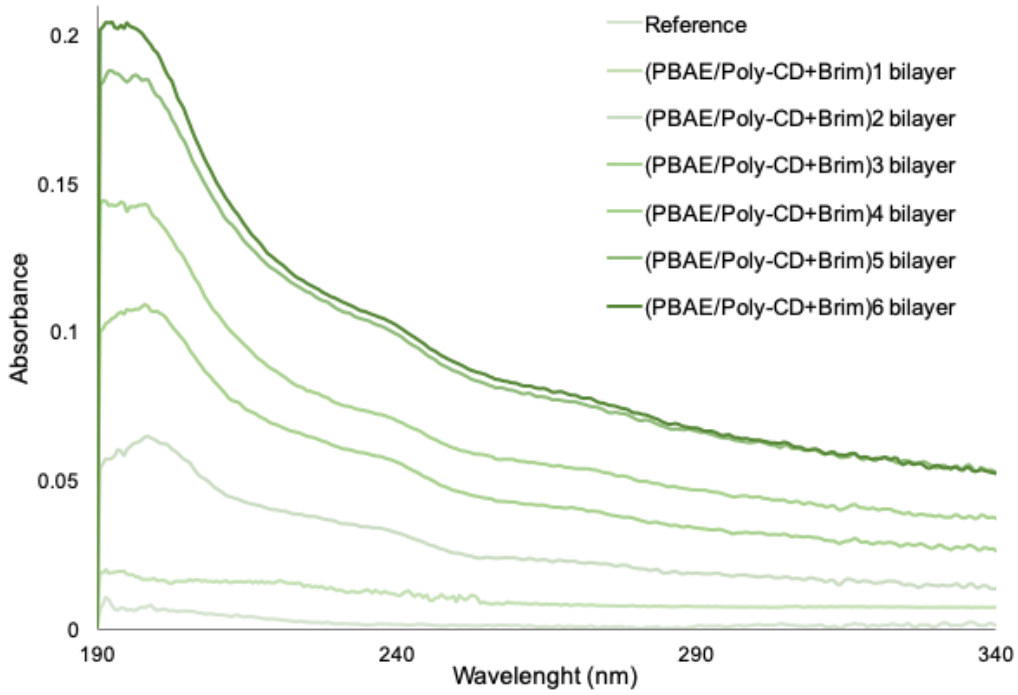

Figure 55 - Absorption spectra of six (PBAE/Poly-CD+Brim) bilayer of the 2st LbL Film, obtained after each bilayer deposition.

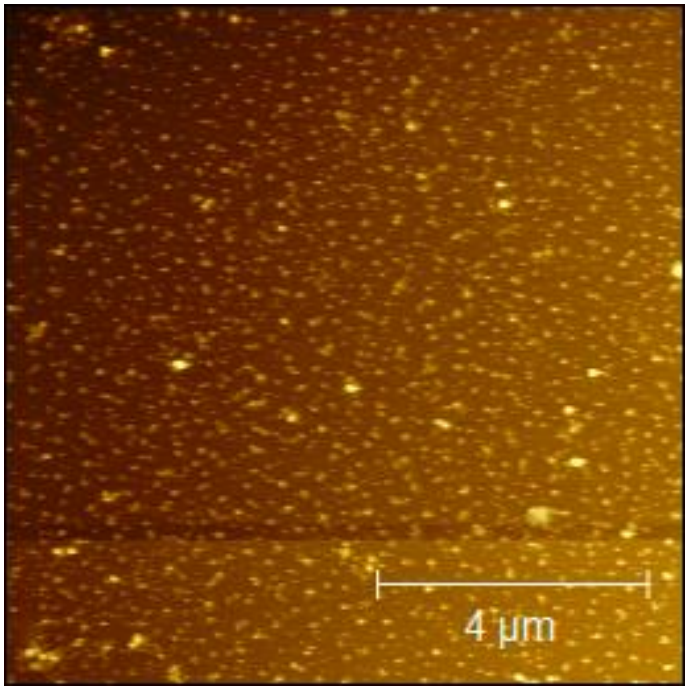

Figure 56 – Topography AFM image with a scan area 10x10 μm^2 $(PBAE/Poly\text{-}CD+Brim)_1$.

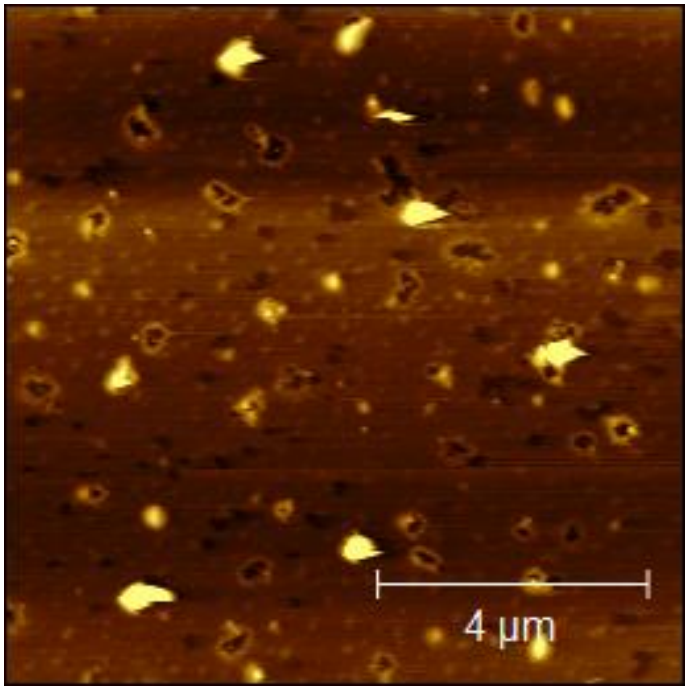

Figure 57 - Topography AFM image with a scan area 10x10 μm^2 $(PBAE/Poly\text{-}CD+Brim)_2$.

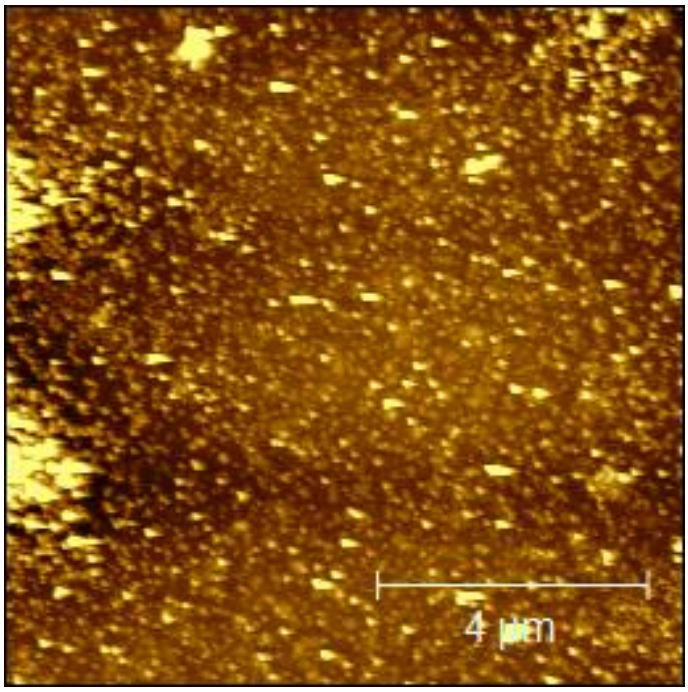

Figure 58 – Topography AFM image with a scan area 10x10 μm^2 $(PBAE/Poly\text{-}CD+Brim)_3$.

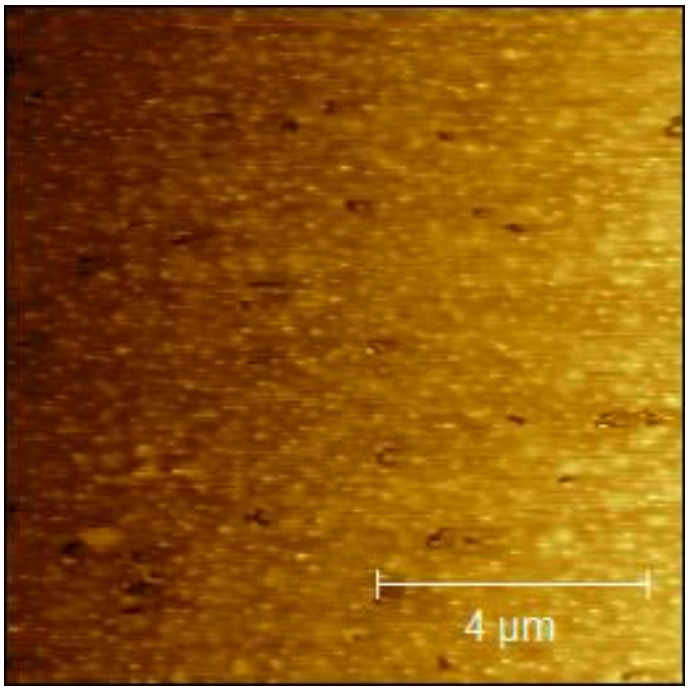

Figure 59 – Topography AFM image with a scan area 10x10 μm^2 $(PBAE/Poly\text{-}CD+Brim)_4$.

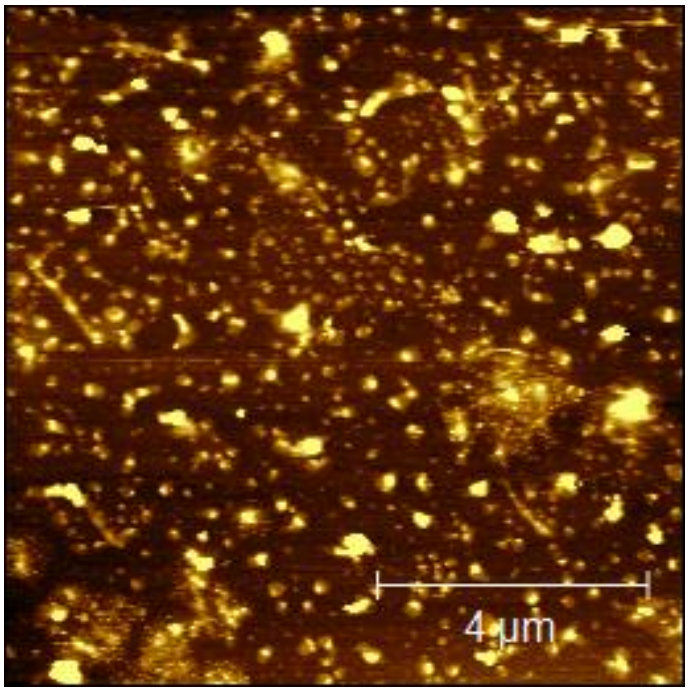

Figure 60 – Topography AFM image with a scan area 10x10 μm^2 $(PBAE/Poly\text{-}CD+Brim)_{5.}$

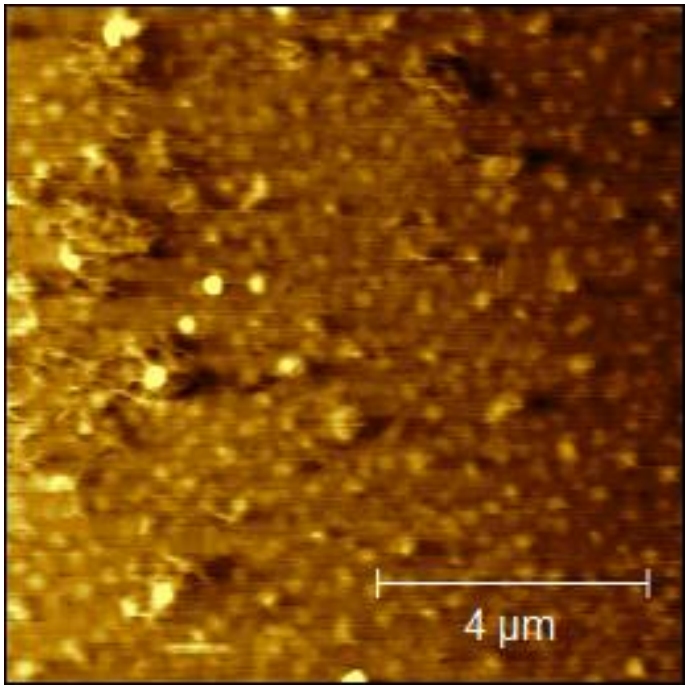

Figure 61 - Topography AFM image with a scan area 10x10 μm^2 $(PBAE/Poly\text{-}CD+Brim)_{6.}$

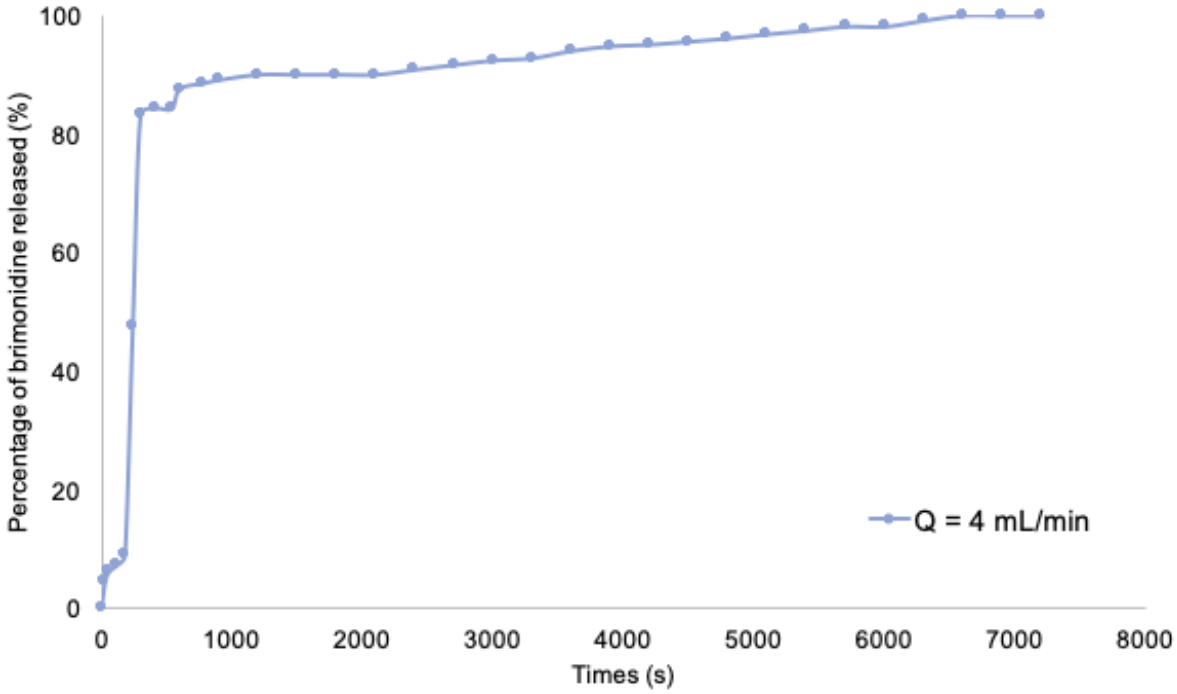

Figure 62 - Normalized values of Brimonidine release kinetics at Q = 4 mL/min for 7200 seconds.

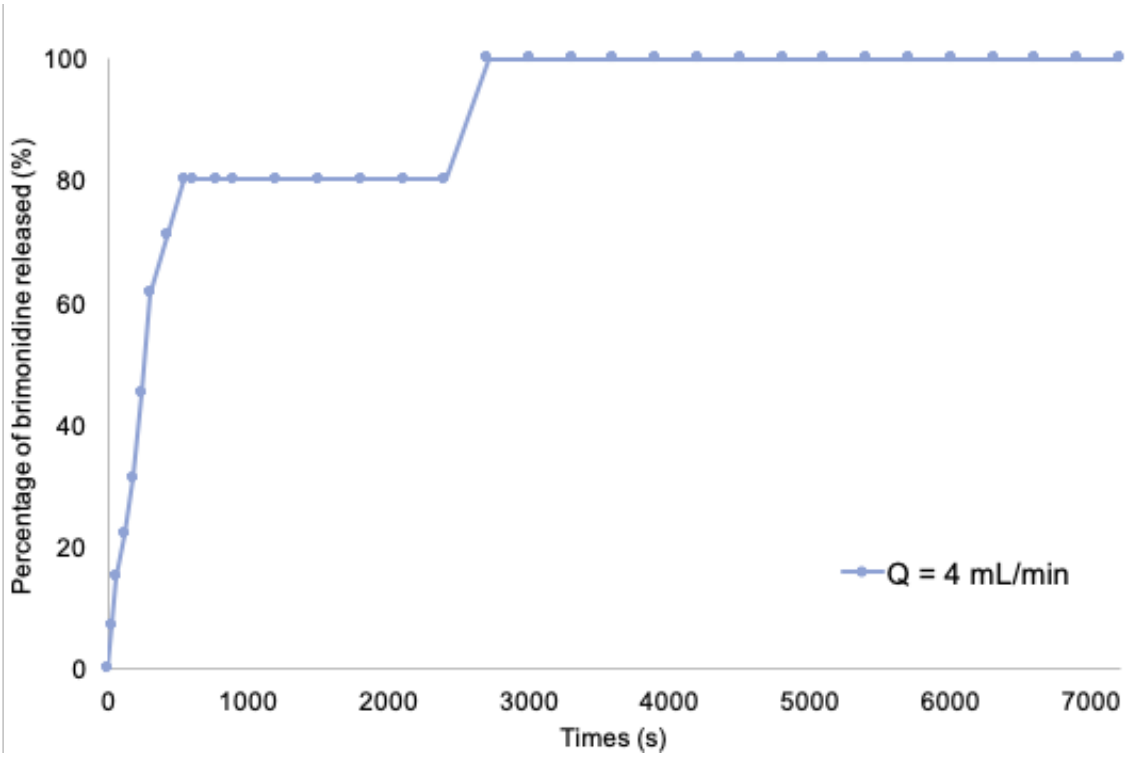

Figure 63 - Normalized values of Brimonidine release kinetics at Q = 4 mL/min for 7200 seconds